

1 **Large fluctuations of shallow seas in low-lying Southeast Asia driven by mantle flow**

2

3 Sabin Zahirovic¹, Nicolas Flament¹, R Dietmar Müller¹, Maria Seton¹, and Michael Gurnis²

4

5 ¹EarthByte Group, School of Geosciences, The University of Sydney, NSW 2006, Australia

6 ²Seismological Laboratory, California Institute of Technology, Pasadena, California 91125, USA

7 Corresponding author: Sabin Zahirovic (sabin.zahirovic@sydney.edu.au)

8

9 **Key Points**

- 10 • Late Cretaceous-Eocene regional unconformity in Southeast Asia likely driven by dynamic
- 11 topography
- 12 • Collision of Gondwana-derived terranes choked subduction and resulted in regional
- 13 dynamic uplift
- 14 • Linked tectonic and mantle flow models highlight influence of plate-mantle system on
- 15 surface processes

16

17

18 Abstract

19 The Sundaland continental promontory, as the core of Southeast Asia, is one of the lowest lying
20 continental regions, with half of the continental area presently inundated by a shallow sea. The role
21 of mantle convection in driving long-wavelength topography and vertical motion of the lithosphere
22 in this region has often been ignored when interpreting regional stratigraphy, including a
23 widespread Late Cretaceous-Eocene unconformity, despite a consensus that Southeast Asia is
24 presently situated over a large-amplitude, dynamic topography low resulting from long-term post-
25 Pangea subduction. We use forward numerical models to link mantle flow with surface tectonics,
26 and compare predicted trends of dynamic topography with eustasy and regional paleogeography to
27 determine the influence of mantle convection on regional basin histories. A Late Cretaceous
28 collision of Gondwana-derived terranes with Sundaland choked the active margin, leading to slab
29 breakoff and a ~10-15 Myr-long subduction hiatus. Slab breakoff likely resulted in several hundred
30 meters of dynamic uplift and emergence of Sundaland between ~80 and 60 Ma, and may explain
31 the absence of a Late Cretaceous-Eocene sedimentary record. Renewed subduction from ~60 Ma
32 reinitiated dynamic subsidence of Sundaland, leading to submergence from ~40 Ma despite falling
33 long-term global sea levels. Our results highlight a complete ‘down-up-down’ dynamic topography
34 cycle experienced by Sundaland, with transient dynamic topography manifesting as a major
35 regional unconformity in sedimentary basins.

36

37 1 Introduction

38 The Indonesian islands and surrounding region represent one of the most low-lying
39 continental areas on Earth with almost half of this region, known as Sundaland, presently inundated
40 by a shallow sea (Figure 1a). The present-day low regional elevation has been attributed to the
41 massive volume of oceanic slabs sinking in the mantle beneath Southeast Asia, leading to regional
42 dynamic subsidence [*Bertelloni and Gurnis, 1997; Spasojevic and Gurnis, 2012*]. However, a Late
43 Cretaceous to Eocene regional unconformity [*Clements et al., 2011; Doust and Sumner, 2007*]

44 indicates that shallow seas retreated following regional flooding during the mid-Cretaceous (Figure
45 1b) sea level highstand [*Haq, 2014; Haq et al., 1987*]. During the Eocene, less than one fifth of
46 Sundaland was submerged (Figure 1c), despite estimates of global sea level being ~200 m higher
47 than at present [*Haq and Al-Qahtani, 2005; Haq et al., 1987*]. Here we use forward models in
48 combination with regional paleogeography and estimates on eustasy to unravel how plate tectonics
49 and mantle convection may have influenced the flooding of Sundaland through time.

50 The post-Pangea tectonic history of Sundaland is dominated by long-lived subduction of
51 oceanic plates, including the Tethyan ocean basins from the south, and the Izanagi and Pacific
52 oceanic plates from the east [*Hutchison, 1975; Katili, 1975; Metcalfe, 1988; Seton et al., 2012*]. The
53 initiation of subduction along southern Eurasia during the Late Jurassic is suggested to have
54 resulted in dynamic subsidence and the deposition of widespread Late Jurassic-Early Cretaceous
55 red beds (Figure 2) across Sundaland [*Clements et al., 2011*]. Independently, mid-Cretaceous
56 greenhouse conditions and a seafloor spreading pulse that produced large areas of young buoyant
57 oceanic seafloor resulted in rising global sea levels [*Seton et al., 2009*], reflected in a number of
58 eustatic sea level curves [*Haq, 2014; Haq and Al-Qahtani, 2005; Haq et al., 1987; Müller et al.,*
59 *2008*]. A regional paleogeographic reconstruction [*Golonka et al., 2006*] suggests that flooding of
60 Sundaland peaked in mid-Cretaceous times between ~120 and 90 Ma (Figure 1b), coincident with
61 rising global sea levels and dynamic subsidence from a well-established subduction zone along the
62 Sundaland margin, leading to the advance of shallow seas on the Sunda Shelf.

63 The East Java and West Sulawesi continental fragments were approaching the Sundaland
64 active margin in the Late Cretaceous, with the lack of volcanic-derived zircons after 80 Ma
65 [*Clements and Hall, 2011*] suggesting the end of subduction in this segment of the margin and
66 suturing of these terranes to the core of Sundaland. Further west, subduction ceased on the Sumatra
67 margin by ~75 Ma as a result of Woyla back-arc closure and intra-oceanic terrane accretion onto
68 Sundaland [*Zahirovic et al., 2014*]. This timing is consistent with a magmatic gap between ~75 and
69 60 Ma on Sumatra, suggesting a ~10–15 Myr hiatus in subduction along this margin [*McCourt et*

70 *al.*, 1996]. These suturing events interrupted subduction along southern Sundaland, and could have
71 induced slab break-off, as has been suggested following continental collisions [*Davies and von*
72 *Blanckenburg*, 1995; *Duretz et al.*, 2014]. Computations in a three-dimensional domain by *van*
73 *Hunen and Allen* [2011] suggest that slab break-off may occur 10–20 Myr after the entry of
74 continental crust into a subduction zone, while the computations of *Li et al.* [2013], also in 3D,
75 highlight the complexity and diachroneity of slab tearing following collision. Since we impose a
76 hiatus in subduction between ~75 and 60 Ma, our method does not capture the geodynamic
77 complexity of slab breakoff. However, our approach allows us to investigate the consequences of a
78 subduction hiatus on the large-scale topography of the overriding plate.

79 Dynamic uplift following slab detachment is thought to be responsible for the widespread
80 emergence of Sundaland and the establishment of erosional regimes from Late Cretaceous to
81 Eocene times, resulting in a regional unconformity across Sundaland [*Clements et al.*, 2011; *Doust*
82 *and Sumner*, 2007] (Figure 3). Large volumes of sediment were transported beyond the continental
83 slope of the Sunda Shelf (Figure 2) – including sediment shed into the accretionary prisms of
84 northern Borneo and southern Java [*Clements and Hall*, 2007]. Importantly, Late Cretaceous to
85 Eocene sediments are missing from almost all Sundaland basins [*Clements et al.*, 2011; *Doust and*
86 *Sumner*, 2007] (Figure 3), and thus the crustal deformation and uplift caused by Late Cretaceous
87 collisions of continental blocks to southern Sundaland are unlikely to be the dominant mechanism
88 responsible for the regional nature of the unconformity. Lithospheric flexure in response to loading
89 by orogenic belts generally results in downwarping inboard of the active continental margin, and
90 the establishment of foreland basins. This would lead to localised flooding in the vicinity of the
91 subduction zone, but not over large continent-wide spatial scales. Moreover, flexural deformation
92 and crustal deformation are typically limited to spatial scales of ~100–200 km [*Buiter et al.*, 2002;
93 *Gurnis*, 1991; *McKenzie*, 2010], whereas wavelengths of mantle-driven topography are typically
94 many hundreds or thousands of kilometres, depending on the depth of density anomalies [*Hager et*
95 *al.*, 1985].

96 Although the long-wavelength dynamic uplift of Sundaland resulting from slab break-off has
97 been proposed conceptually [*Clements et al.*, 2011], here we explicitly test such a scenario in the
98 context of plate tectonics, geodynamics, paleogeography and the role of long-term changing sea
99 levels in modifying the long-term flooding and emergence of Sundaland. We use 4D (3D space, and
100 time) global mantle flow numerical models [*Bower et al.*, 2015; *Flament et al.*, 2014] coupled with
101 regionally-refined global plate reconstructions [*Zahirovic et al.*, 2014] to investigate the space-time
102 evolution of dynamic topography associated with the history of slab breakoff and subduction re-
103 initiation, and the response of the overriding Sundaland continent.

104

105 **2 Methods**

106 **2.1 Flooding extent from paleogeographic reconstructions**

107 Paleogeographic maps that are constructed from detailed regional syntheses of paleo-facies
108 distributions provide a powerful insight into the shifting depositional (and erosional) environments
109 deep in geological time. A detailed paleogeographic map for Borneo and Sulawesi exists only for
110 the Cenozoic [*Wilson and Moss*, 1999], but not for the rest of Sundaland back to the Cretaceous. A
111 synthesis of basin sedimentary histories across Southeast Asia [*Doust and Sumner* [2007] provides
112 a deeper time and wider spatial context for depositional regions (Figure 3 and 4). The
113 paleogeographic maps of *Golonka et al.* [2006] are paleo-environmental reconstructions for both
114 erosional and depositional regions, in a plate tectonic context for the entire Southeast Asia region
115 (Figure S2), that span our model timeframe, as well as the entire Phanerozoic. We georeferenced
116 paleogeographic reconstructions of Southeast Asia from *Golonka et al.* [2006] and converted paleo-
117 environments to categories of oceanic crust, inundated continental crust and emergent continental
118 crust (Figure 5). For the purpose of calculating areas of inundation and emergence, the polygons
119 representing the paleogeographies were reprojected into an equal-area cylindrical co-ordinate
120 system with a central meridian of 110°E and a standard parallel of 0°N, suitable for the near-
121 equatorial positions of Sundaland since the Jurassic. Paleogeographic snapshots in geological stages

122 with ~10–20 Myr temporal intervals are informative for the long-term geography of Sundaland, and
123 appropriate for comparisons with long-term sea level trends and topography evolution.

124 We calculated the long-term flooding of Sundaland from the area of inundated continental
125 crust in the paleogeographic reconstructions (Figure 5). The extent of Sundaland includes
126 Indochina, Sibumasu, the Malay Peninsula, Sumatra and Borneo, that have existed as a welded
127 continental block since the Jurassic, albeit with tectonically-reactivated boundaries following the
128 propagating effects of the India-Eurasia collision [Hall, 2002; Lee and Lawver, 1995]. The
129 continental portions of East Java and West Sulawesi were added following their accretion to
130 Sundaland by ~80 Ma, as well as the accretion of Woyla arc material to Sumatra by ~75 Ma
131 [Zahirovic *et al.*, 2014].

132

133 **2.2 Plate tectonics and geodynamics of Sundaland**

134 We model global mantle flow based on the subduction history predicted by a global tectonic
135 reconstruction [Seton *et al.*, 2012] with refinements for Southeast Asia [Zahirovic *et al.*, 2014] that
136 are embedded in a recent global synthesis [Müller *et al.*, 2016] (see Digital Supplement). Viscous
137 mantle flow is computed using CitcomS [Zhong *et al.*, 2008] and is driven by plate velocities
138 (Figure 6) applied as time-dependent boundary conditions while the thermal structure of lithosphere
139 and slabs are progressively assimilated in 1 Myr intervals from the plate reconstructions following
140 Bower *et al.* [2015].

141 In the initial condition at 230 Ma, a thermochemical layer 113 km thick at the base of the
142 mantle is assumed, in which material is 3.6% denser than ambient mantle. This set up suppresses
143 the formation of mantle plumes, which allows subduction-driven dynamic topography to be isolated
144 [Flament *et al.*, 2014]. The temperature and thickness of the lithosphere is derived using a half-
145 space cooling model and the synthetic age of the ocean floor [Bower *et al.*, 2015]. The global
146 thermal structure of slabs is based on the location of subduction zones and on the age of the
147 adjacent ocean floor [Bower *et al.*, 2015]. In the initial condition, slabs are inserted down to

148 1,400 km depth, with a dip of 45° down to 425 km depth and a dip of 90° below 425 km.
 149 Subduction zones thought to have initiated just prior to 230 Ma are inserted to a depth based on
 150 their subduction duration and assuming a descent rate of 3 and 1.2 cm/yr in the upper and lower
 151 mantle, respectively. Slabs are initially twice as thick in the lower mantle than in the upper mantle
 152 to account for advective thickening. Subduction zones that appear during the model run are
 153 progressively inserted in the upper mantle. The global thermal structure of the lithosphere and of
 154 subducting slabs is inserted in the dynamic models at 1 Myr increments, to a depth of up to 350 km
 155 at subduction zones [Bower *et al.*, 2015].

156 The Rayleigh number is defined as

$$157 \quad Ra = \frac{\alpha_0 \rho_0 g_0 \Delta T h_M^3}{\kappa_0 \eta_0}, \quad (1)$$

158 where α is the coefficient of thermal expansivity, ρ the density, g the acceleration of gravity, ΔT the
 159 temperature change across the mantle, h_M is the thickness of the mantle, κ the thermal diffusivity, η
 160 the viscosity, and the subscript “0” indicates reference values. Values are listed in Table 1.

161 The viscosity of the mantle depends on pressure and temperature (Figure 7) following:

$$162 \quad \eta = \eta_0(r) \exp \left(\frac{E_\eta}{R(T+T_\eta)} - \frac{E_\eta}{R(T_b+T_\eta)} \right) \quad (2)$$

163 where $\eta_0(r)$ is a pre-factor defined with respect to the reference viscosity η_0 for four layers: it is
 164 equal to 1 above 160 km, either to 1 (for cases without asthenosphere, see Table 2) or to 0.1 (for
 165 cases with an asthenosphere, see Table 2) between 160–310 km depth, to 1 between 310–660 km
 166 depth and either to 100 or linearly increasing from 10 to 100 in the lower mantle below 660 km
 167 depth (see Table 2). E_η is the activation energy (E_{UM} in the upper mantle and E_{LM} in the lower
 168 mantle), R is the universal gas constant, T is the dimensional temperature, T_η is a temperature offset,
 169 and T_b is the ambient mantle temperature (values are listed in Table 1). The average model
 170 resolution, obtained with $\sim 13 \times 10^6$ nodes and radial mesh refinement, is $\sim 50 \times 50 \times 15$ km at the
 171 surface, $\sim 28 \times 28 \times 27$ km at the core–mantle boundary (CMB), and $\sim 40 \times 40 \times 100$ km in the mid-
 172 mantle.

173 We present mantle evolution from the latest Jurassic (~160 Ma), from which time the plate
174 reconstructions in *Zahirovic et al.* [2014] are regionally refined (Figure 6 and 8), and extract the
175 average dynamic topography acting on Sundaland from the Late Cretaceous (100 Ma) to present.
176 The dynamic topography h is obtained by scaling the total normal stress σ_{rr} on the top model
177 surface following:

$$178 \quad h = \frac{\sigma_{rr}}{\Delta\rho g_0}, \quad (3)$$

179 where $\Delta\rho$ is the density difference between the shallow mantle $\rho_{UM} = 3340 \text{ kg m}^{-3}$ and sea water
180 ($\rho_w = 1030 \text{ kg m}^{-3}$), R_0 is the radius of the Earth and other parameters are listed in Tables 1 and 2.
181 Water-loaded dynamic topography is calculated from the vertical stress resulting from mantle flow
182 in restarts of the main calculation with free-slip boundary conditions while ignoring buoyancy and
183 lateral viscosity variations above 350 km depth, which is the maximum depth to which subducting
184 slabs are inserted using time-dependent upper boundary conditions [see *Bower et al.*, 2015 for
185 details]. As a result, we cannot model slab breakoff, and instead focus on the role of a subduction
186 hiatus that we infer from a ~75 to 61 Ma magmatic gap on Sumatra. Four model cases were run to
187 test the sensitivity of the results to the choice of radial viscosity profile and absolute plate motion
188 model (Table 1, Figure 7). Cases 1, 3 and 4 incorporate a low-viscosity asthenosphere, unlike Case
189 2. The radial viscosity is uncertain and so, we test end-member profiles, with either a one- or two-
190 order of magnitude increase in viscosity in the lower mantle with respect to the mantle transition
191 zone (Case 1 and 2, respectively). In Case 3 and 4 we implement a progressive increase in viscosity
192 from a factor of 10 at the base of the transition zone to a factor of 100 deeper in the lower mantle
193 (10→100 in Table 2), following *Steinberger and Calderwood* [2006]. To test the influence of the
194 absolute reference frame for plate motions, we apply the subduction-calibrated longitudinal
195 positions from *van der Meer et al.* [2010] in Case 3, and a moving hotspot frame from *Torsvik et al.*
196 [2008] and a True Polar Wander-corrected reference frame based on *Steinberger and Torsvik*
197 [2008] for earlier times, as described in *Seton et al.* [2012] and *Müller et al.* [2016], for the other
198 cases.

199

200 **3 Results**201 **3.1 Comparison of present-day predictions to residual topography and seismic**
202 **tomography**

203 Predictions of present-day dynamic topography can be compared with estimates of residual
204 topography taken from the synthesis of *Winterbourne et al.* [2014]. The dynamic topography for
205 Southeast Asia is superimposed with point-estimates of residual topography (colored circles and
206 triangles in Figure 9). A perfect fit between predicted dynamic topography and observed residual
207 topography would result in a slope of 1, assuming that all or most of the residual topography is due
208 to dynamic topography. Keeping in mind the scarcity of residual topography estimates, we assess
209 which mantle viscosity and tectonic histories give the smaller RMS distance between predicted
210 dynamic topography and residual topography.

211 The present-day amplitude and spatial distribution of predicted dynamic topography across
212 Southeast Asia are generally consistent with available constraints on residual topography
213 [*Winterbourne et al.*, 2014], as reflected by a root-mean-square (RMS) distance of ~250 to 300 m
214 between predictions (dynamic topography ranging between approximately -1600 and 0 m across all
215 models) and constraints (residual topography ranging between approximately -1800 and +200 m).
216 Assumptions underlying the estimates of residual topography by *Winterbourne et al.* [2014] used
217 here include a model for the cooling of the oceanic lithosphere, and a model for the seismic velocity
218 of sedimentary columns in the oceans. As with standard deviations, predicted versus observed
219 values within one RMS error (grey lines – Figure 9) are assumed to represent a good fit and are
220 plotted as circles. Acceptable values, within two RMS errors (dashed grey lines – Figure 9), are
221 plotted as upright triangles. Between 62 and 72% of predictions fall within one RMS across model
222 cases (Figure 9). One value in the Bengal Fan region (BF, Figure 9b), and one to two values in the
223 Pacific (Figure 9a–d) are outside the acceptable errors (plotted as inverted triangles). However,
224 these may be outliers in the *Winterbourne et al.* [2014] compilation due to high corrections for

225 sediment thicknesses. Discrepancies between predicted dynamic topography and estimates of
226 residual topography could also reflect that sources of buoyancy and lateral viscosity variations are
227 ignored in the top 350 km of the mantle in the calculation of dynamic topography, although the
228 shallow mantle is expected to be a source of short-wavelength dynamic topography [*Colli et al.*,
229 2016; *Hoggard et al.*, 2016]. The match between residual and dynamic topography is comparatively
230 better for Case 2 than the other models, with an RMS value of ~249 m and 72% of residual
231 topography values in overall agreement with the dynamic topography prediction. The better match
232 to residual topography in Case 2 is largely due to the lower amplitude of the predicted dynamic
233 topography, in which the model has a viscosity jump of 100 from the upper to lower mantle (Figure
234 7). Although the other cases predict higher dynamic topography amplitudes, the regional and time-
235 dependent trends (see Section 3.2) that are the key to our interpretations are consistent between
236 models.

237 The predicted present-day mantle temperature is qualitatively compared to P- and S-wave
238 seismic tomographic models, assuming that seismic velocity anomalies largely result from thermal
239 perturbations [*Becker and Boschi*, 2002; *Grand*, 2002]. The tomographic models share first-order
240 similarities, but differ on scales smaller than several hundred kilometres. This is due to the
241 earthquake sources used, earthquake relocations applied, the crustal correction and model
242 parameterization [*Grand*, 2002; *Romanowicz*, 2008]. Although the P-wave models result in higher
243 resolution imaging of subduction zones and the mantle beneath continents, their resolution and
244 coverage of oceanic regions is more limited than S-wave models [*Romanowicz*, 2003; 2008]. The
245 Sunda slab has been consistently interpreted as a north-dipping feature to a depth of ~1500 km in
246 the mantle beneath the Sundaland continental promontory in P-wave tomography models
247 [*Widiyantoro and van der Hilst*, 1996]. Other post-Jurassic Tethyan slabs related to subduction at
248 the Sunda margin are beneath oceanic regions, that are likely best-sampled by S-wave tomographic
249 models.

250 The highest resolution models for the area are the P-wave models, including MIT-P [*Li et*
251 *al.*, 2008] (Figure 9c) and GAP_P4 [*Obayashi et al.*, 2013]; these models are supplemented by S-
252 wave models that provide more uniform sampling of the lower mantle [*Romanowicz*, 2003],
253 including S40RTS [*Ritsema et al.*, 2010] and GRAND-S [*Grand*, 2002] (Figure 10). Our numerical
254 models (Cases 1–4) are compatible with the first-order mantle structure interpreted from P- and S-
255 wave tomography (Figure 10), including the positions of the upper- to mid-mantle Sunda slab and
256 the lower mantle Meso-Tethyan and East Asian slabs (Figure 10). Importantly, the Late Cretaceous
257 subduction hiatus along southern Sundaland reproduces the gaps in the slab at the expected depths
258 including the mid mantle (~1500 km) and lower mantle (~2000 km, Figure 10) in Cases 2 and 4.
259 Case 2 predicts the correct depth of the Sunda slab, and better matches residual topography than the
260 other cases. We note that all our cases predict the Sunda slab using a range of mantle viscosity
261 profiles and alternative absolute plate motion models. Although an assumption of vertical slab
262 sinking would infer that the lower mantle slab material is purely from the Jurassic-Cretaceous
263 Sundaland active margin, our time-dependent mantle flow models suggest that slabs are both from
264 Tethyan and East Asian subduction (Figure 8).

265

266

267

3.2 Comparison between time-dependent predictions and the geological record

268 The Mesozoic flooding history of Southeast Asia is characterised by episodes of advancing
269 and retreating shallow seas (Figure 11a). The regional sedimentary record is a key constraint
270 indicating past regional flooding, such as the mid Cretaceous Eromanga and Surat basins of eastern
271 Australia, and is therefore crucial for interpreting the dynamic topography from mantle flow models
272 [*Gurnis et al.*, 1998]. Mantle flow models show a regional prevalence of negative dynamic
273 topography associated with Tethyan subduction along the southern Sundaland margin, and Izanagi
274 and (proto-) Pacific subduction to the north and east (Figure 8). However, following suturing of the
275 Woyla terranes and the West Sulawesi-East Java continental blocks to Sundaland between ~80–
276 75 Ma [*Clements and Hall*, 2011; *Zahirovic et al.*, 2014], the region experienced broad dynamic

277 uplift as a consequence of subduction cessation (Figure 8 and 11b). The magmatic gap from ~75 to
278 61 Ma on Sumatra [McCourt *et al.*, 1996] is consistent with Woyla accretion and subduction
279 cessation, while the resumption of arc volcanism by ~60 Ma indicates renewed subduction along
280 the entire Sundaland southern margin. Regional dynamic subsidence was re-established from
281 ~40 Ma (Figures 8, 11b and 12), as negatively buoyant slabs sank in the upper mantle. This
282 ~20 Myr lag time between subduction initiation and the development of a widespread dynamic
283 topographic low on Sundaland is caused by the time taken for the upper mantle to be populated with
284 sinking slabs from circum-Sundaland subduction. Although the absolute values for dynamic
285 topography are sensitive to the radial viscosity structure (Figure 12), and to a lesser extent the
286 absolute plate motion reference frame, the regionally-averaged dynamic topography trends are
287 common to all models, which highlights the control of the subduction history on the dynamic
288 topography trends for Sundaland (Figure 11b). We compute the dynamic topography considering
289 sources of buoyancy deeper than 250 km (Figure 12, dashed green line), to verify that the timing of
290 dynamic uplift and subsidence for Sundaland remain consistent with the dynamic topography
291 derived from sources of buoyancy deeper than 350 km.

292

293 **4 Discussion**

294 The mantle beneath Southeast Asia has been dominated by post-Pangea subduction with long-
295 term convergence between Eurasian, Indo-Australian and Pacific plates. Seismic tomography of the
296 mantle provides crucial clues in untangling the complex history of plate motions that led to the
297 present-day labyrinthine network of suture zones and plate boundaries in Southeast Asia [Hall and
298 Spakman, 2015; Wu *et al.*, 2016]. By comparing plate reconstructions in a Siberia-fixed reference
299 frame with depth slices of P-wave seismic tomography, Replumaz *et al.* [2004] interpreted the
300 nature and timing of key changes in the geodynamic evolution of Southeast Asia, and inferred links
301 between surface tectonics and mantle evolution. Their interpretations suggested an average slab
302 sinking rate of 5 and 2 cm/yr in the upper and lower mantle, respectively, and the onset of India-

303 Eurasia continental collision at ~55–40 Ma. The dip of the Sunda slab beneath Sundaland is
304 interpreted by *Replumaz et al.* [2004] to result from ~5–10° southward slab rollback since ~50 Ma,
305 however, the assumed plate reconstructions in *Replumaz et al.* [2004] do not model the south-
306 dipping subduction of the Proto South China Sea along northern Borneo since ~50 Ma [*Hutchison,*
307 1996; *Soeria-Atmadja et al.*, 1999; *Zahirovic et al.*, 2014] and do not accommodate oroclinal
308 bending of Sundaland [*Hutchison*, 2010; *Zahirovic et al.*, 2014]. The oroclinal bending was likely
309 responsible for the ~50° counter-clockwise rotation of Borneo since 25 Ma [*Fuller et al.*, 1999],
310 which influenced the evolution of the Sunda Trench, while the subduction of the Proto South China
311 Sea is an additional factor required in interpreting the present-day Sunda slab structure.

312 The work of *Káráson* [2002] applied a similar approach and interpretation as *Replumaz et al.*
313 [2004] and modeled the evolution of the Sunda slab using an analytical Stokes flow solution using a
314 swarm of ‘slablets’ in a regional framework where the time-dependent position of the southward-
315 retreating Sunda Trench was applied in the surface boundary condition. The prediction of the slab
316 structure was filtered using synthetic seismic tomography, providing a better comparison between
317 predicted slab structure and tomography. Our approach is somewhat similar to the time-dependent
318 incorporation of the subduction zone location on the surface as in the model in *Káráson* [2002], but
319 differs significantly in the modelling approach. First, the analytical solution in *Káráson* [2002] does
320 not take into account temperature-dependence of viscosity and does not solve the energy equation.
321 Second, the model of *Káráson* [2002] is regional, and begins with a pristine mantle at ~50 Ma, and
322 third, such an approach does not incorporate variable convergence rates or lithospheric thickness of
323 the downgoing plate. In contrast, our global geodynamic models incorporate more realistic mantle
324 and slab rheologies and allow us to track the origin and trajectory of slabs in the mantle. However,
325 the work of *Káráson* [2002] presented an important development in linking tectonic reconstructions
326 of Southeast Asia to mantle evolution and the present-day mantle structure from seismic
327 tomography.

328 Sundaland's post-Jurassic long-wavelength topography has been influenced by the evolution
329 of regional subduction zones in addition to the effect of changing global sea levels. Long-term
330 global sea level change plays a significant role in the advance and retreat of marine environments
331 across continental shelves [*Gurnis, 1993; Haq et al., 1987*], and is therefore an important driving
332 mechanism to consider for the flooding and emergence of Sundaland. However, our results suggest
333 that dynamic topography played an important role in the long-term emergence and inundation of
334 Sundaland since the Late Cretaceous. Our analysis is based on long-term sea level chronologies
335 derived from sea level highstands (Figure 11a), representing the first- and second-order sea level
336 cycles (several to many millions of years) related to large-scale tectonics [*Lovell, 2010; Vail et al.,*
337 *1977*], which are applicable to the long-term paleogeographic analysis of Sundaland flooding.
338 Although a number of eustatic sea level curves exist, we favour sea level histories derived globally
339 [*Spasojevic and Gurnis, 2012*] rather than locally because global estimates of sea level are not
340 strongly influenced by regionally-transient dynamic topography [*Conrad and Husson, 2009;*
341 *Moucha et al., 2008; Müller et al., 2008; Spasojevic and Gurnis, 2012*]. For example, the long-term
342 relative sea level curve derived from the Arabian Platform in *Haq and Al-Qahtani [2005]* shares
343 major trends with the eustatic sea level curve from *Haq et al. [1987]* (Figure 11a), but shows the
344 potential role of regional factors (including dynamic topography) that cause such regional curves to
345 deviate from global trends.

346 The flooding of Sundaland between ~100 and 80 Ma is likely due to high eustatic sea levels
347 [*Haq, 2014; Haq et al., 1987*] amplified by dynamic subsidence from post-Jurassic subduction
348 [*McCourt et al., 1996; Zahirovic et al., 2014*]. However, the predicted dynamic topography trends
349 alone reproduce the timing of shallow sea retreat from ~80 to 60 Ma, as well as the subsequent
350 flooding from ~40 Ma (Figure 11b). This is in contrast with the long-term sea level trend, which is
351 largely falling since ~30 Ma and is out of phase with the inundation of Sundaland. Thus, regional
352 dynamic uplift during Late Cretaceous to Eocene times is a plausible mechanism for Sundaland
353 emergence and the establishment of a contemporaneous regional unconformity. Renewed dynamic

354 subsidence from ~40 Ma, along with the onset of rifting in many Sundaland basins, plays an
355 important role in the long-term advance of shallow seas on the Sunda Shelf while rapidly falling
356 global sea levels from ~15 Ma partly offset this flooding and result in widespread regressive deltaic
357 sedimentation from mid-Miocene times [*Doust and Sumner, 2007*] (Figure 3 and 4).

358 In addition, the interaction of the Wharton Ridge with the Sunda active margin (Figure 4), and
359 the resulting slab window [*Whittaker et al., 2007*], may play a role in moderating the subduction-
360 induced dynamic subsidence. In our plate reconstructions the Wharton Ridge sweeps progressively
361 westwards across the Sunda active margin from ~60 Ma near Java until it is abandoned at ~40 Ma
362 adjacent to Sumatra. The proximity of the Wharton Ridge at ~60–55 Ma to eastern Sundaland is
363 contemporaneous with the onset of rifting in the Barito and Lombok basins along eastern
364 Sundaland, with a generally westward progression of basin rift activation in Sundaland (Figure 4,
365 Animation S1). This pattern of basin activations is consistent with oroclinal bending of Sundaland
366 [*Hutchison, 2010; Zahirovic et al., 2014*], with a potential role of thermal weakening of Sundaland
367 lithosphere and crust from a Wharton Ridge slab window. However, the geodynamic models only
368 predict a moderating effect of the Wharton Ridge on dynamic topography, with slightly weaker
369 dynamic subsidence for central and eastern Sundaland at ~48 Ma (Figure 8d). Our numerical
370 experiments of mantle flow are subduction-driven, and since plumes are suppressed, the resulting
371 dynamic topography only represents the influence of sinking slabs in the mantle and the large-scale
372 mantle upwellings elsewhere. As a result, the subduction history dominates the dynamic topography
373 acting on Sundaland in our models, with second order effects such as the Wharton Ridge slab
374 window moderating the amplitude of the long-wavelength topography.

375 The timeframe of the regional unconformity likely represents an extended period of erosion or
376 non-deposition, with any eroded sediments likely deposited in the Eocene-Miocene Crocker Fan on
377 northern Borneo [*Clements and Hall, 2007; Clements and Hall, 2011*], where the largest volume of
378 Paleogene sediments of Southeast Asian origin have been preserved in a single basin (Figure 2).
379 The zircon age-spectra from the sediments confirm a distal Sundaland source, including the

380 Cretaceous-age Schwaner (southwest Borneo) and the Permo-Triassic (Malay-Thai) Tin Belt
381 granitoids [*van Hattum et al.*, 2006], which were eroded during the Late Cretaceous to Eocene
382 regional dynamic uplift. To the south, reworked pre-Cenozoic sediments, including sediments
383 sourced from Southwest Borneo, were shed into a prograding deltaic system along Java to form the
384 Ciemas and Bayah Formations (Figure 2) during the Eocene [*Clements and Hall*, 2007]. The Late
385 Cretaceous to Eocene unconformity (Figure 3) on Sundaland itself provides no clues for the onset
386 of the erosional event, while the resumption of Eocene-Oligocene sedimentation records post-
387 Eocene rifting in the Gulf of Thailand, Natuna Basins and Java Sea [*Doust and Sumner*, 2007]
388 during which subsidence was enhanced by stronger negative dynamic topography. Our plate
389 reconstructions linked to numerical mantle flow models suggest that dynamic uplift started in the
390 Late Cretaceous, sometime between ~80 and 65 Ma, based on a hiatus in subduction-related
391 volcanism on Sumatra, Java and Borneo [*Clements and Hall*, 2011; *McCourt et al.*, 1996; *Zahirovic*
392 *et al.*, 2014]. Although our approach does not capture the dynamics of slab breakoff, we expect that
393 a ~15 Myr interruption in subduction would have resulted in dynamic uplift in the overriding plate,
394 as occurs in our models. However, since our computation of dynamic topography excludes the
395 contributions of the shallowest ~350 km mantle depths, our modelling does not capture the full
396 response of the crust and lithosphere to slab breakoff. Our results are therefore only relevant for the
397 influence of large-scale mantle flow for Sundaland, and more work is required to isolate the role of
398 crustal, lithospheric and shallow-mantle processes during slab breakoff.

399 The method presented in this study uses a rigid plate motion model for Southeast Asia, with
400 only implied continental deformations, such as the extrusion of Indochina and the oroclinal bending
401 of Borneo [*Zahirovic et al.*, 2014]. Recent work has used this rigid plate motion model as a starting
402 point in constructing a deforming plate reconstruction for Sundaland [*Yang et al.*, 2016]. The
403 deforming plate reconstruction is incorporated into a backward advection model for the last 50 Myr
404 (approx. Eocene), with the present-day mantle structure taken from the RUM slab model
405 [*Gudmundsson and Sambridge*, 1998] and seismic tomography from S40RTS [*Ritsema et al.*,

406 2011]. The backward advection method applied by *Yang et al.* [2016] also reports dynamic
407 subsidence since the Eocene resulting from a slab avalanche, with a larger prediction of subsidence
408 of up to ~400 m since ~40 Ma. In addition, they suggest that basin subsidence and
409 contemporaneous basin inversion can result from an avalanching Sunda slab. Since the amplitude of
410 past dynamic topography is difficult to constrain, we focus on the trends (Figure 11b) rather than
411 the absolute values (Figure 12), as the trends highlight major changes in the regional dynamic uplift
412 or subsidence. The benefit of backward advection models is that they incorporate the present-day
413 mantle structure from seismic tomography as an initial condition, contrary to our models that are
414 agnostic of the present-day mantle structure. However, since backward advection techniques are
415 limited to the last ~75 Ma [*Bunge et al.*, 2003; *Conrad and Gurnis*, 2003], we apply a forward
416 modelling approach to study the longer-term evolution of dynamic topography for Southeast Asia.
417 Future work should focus on coupling mantle flow with lithospheric- and crustal-scale deformation
418 and surface process models to better quantify the relative contributions from mantle, lithosphere,
419 crustal, surface and eustatic mechanisms.

420

421 **5 Conclusions**

422 A Late Cretaceous collision of Gondwana-derived terranes [*Clements et al.*, 2011; *Zahirovic*
423 *et al.*, 2014] resulted in regional dynamic uplift and emergence due to a ~10–15 million-year-long
424 subduction hiatus along the Sunda active margin [*McCourt et al.*, 1996]. Regional dynamic uplift
425 can account for the absence of sediment deposition across Sundaland and the emergence of
426 Sundaland between ~80–60 Ma. Renewed subduction from ~60 Ma reinitiated dynamic subsidence
427 of Sundaland, amplified by active rifting in a number of basins, leading to submergence from
428 ~40 Ma despite decreasing long-term global sea levels [*Haq and Al-Qahtani*, 2005; *Haq et al.*,
429 1987; *Spasojevic and Gurnis*, 2012]. Our results show that Sundaland experienced a complete
430 ‘down-up-down’ dynamic topography cycle over the last 100 million years, with the transience of
431 topography revealed in sedimentary basin stratigraphy punctuated with regional unconformities; our

432 explicit connection to observations is consistent with the theoretical prediction of *Burgess and*
433 *Gurnis* [1995] that dynamic topography should contribute to generating unconformities over long
434 periods of geological time. Subduction-driven mantle convection models can be useful to interpret
435 the geological record of basins, with major regional trends providing insights into episodes of
436 dynamic uplift and subsidence, enabling a deeper understanding of the driving forces of Earth's
437 ephemeral coastlines.

438 By comparing geological data and global sea level evolution with predictions of 4D global
439 mantle flow models, we show that the subduction history had a strong influence over the long-term
440 flooding and emergence of Southeast Asia on geological timescales. Our model may explain the
441 timing of the Late Cretaceous-Eocene major regional unconformity on Sundaland, and may also
442 account for the present-day distribution of residual topography and mantle structure. Our results
443 capture an entire cycle of dynamic uplift and subsidence that caused an advance, retreat and re-
444 advance of shallow marine environments on Sundaland. This process may apply to other
445 continental regions that have experienced punctuated episodes of subduction. Predictions of the
446 long-term evolution of long-wavelength topography could be coupled with surface process models
447 to understand how erosion links low-amplitude and long-wavelength dynamic uplift to regional
448 unconformities [*Braun et al.*, 2013; *Burgess and Gurnis*, 1995; *Clements et al.*, 2011] and
449 associated pulses of deposition in sedimentary basins. More generally, there is a need for methods
450 to assess the dynamic contribution to regional sea level curves, as well as a need for new methods in
451 linking mantle and surface processes across wide spatial and temporal scales.

452

453

454

455

456

457

458 **Tables**

459

460

461 **Table 1.** Parameters common to all model cases. Subscript “0” denotes reference values.

Parameter	Symbol	Value	Units
Rayleigh number	Ra	7.84×10^7	–
Thermal expansion coefficient	α_0	3×10^{-5}	K^{-1}
Density	ρ_0	4000	kg m^{-3}
Gravity acceleration	g_0	9.81	m s^{-2}
Temperature change	ΔT	2825	K
Temperature offset	T_η	452	K
Background mantle temperature	T_b	1685	K
Mantle thickness	h_M	2867	km
Earth radius	R_0	6371	km
Universal gas constant	R	8.31	$\text{J mol}^{-1} \text{K}^{-1}$
Thermal diffusivity	κ_0	1×10^{-6}	$\text{m}^2 \text{s}^{-1}$
Reference Viscosity	η_0	1×10^{21}	Pa s
Activation energy (upper mantle)	$E_{\eta UM}$	100	kJ mol^{-1}
Activation energy (lower mantle)	$E_{\eta LM}$	33	kJ mol^{-1}
Activation temperature	T_η	452	K

462

463

464

465 **Table 2.** Parameters for numerical mantle flow models in Case 1–4.

	Case 1	Case 2	Case 3	Case 4
Mesh nodes			129 × 129 × 12 (nodes on the surface) × 65 (depth levels)	
Viscosity relative to Reference Viscosity (Lithosphere, Upper mantle/Asthenosphere, Transition zone, Lower Mantle)	1,0.1,1,100	1,1,1,100	1,0.1,1,10→100 following <i>Steinberger and Calderwood</i> [2006]	1,0.1,1,10→100
Plate reconstruction	<i>Zahirovic et al.</i> [2014]		Reconstructions from <i>Zahirovic et al.</i> [2014] with subduction-calibrated longitudinal positions from <i>van der Meer et al.</i> [2010]	<i>Zahirovic et al.</i> [2014]

466

467

468

469

470 **Figure Captions**

471 **Figure 1.** Long-term continental inundation of Sundaland. (a) About 42% of Sundaland continental
472 area is flooded at present, which is similar to (b) the mid-Cretaceous. In contrast, the continental
473 promontory was emergent for much of the Eocene (c), a period marked by erosional environments
474 corresponding to a widespread regional unconformity [*Clements et al.*, 2011]. Past inundation
475 patterns were deduced from paleogeographic reconstructions of *Golonka et al.* [2006]. Oceanic
476 crust (dark blue) is not included in the calculation of inundation. BOR, Borneo (Schwaner Core);
477 CF, Crocker Fan; Ci-Ba, Ciemas and Bayah Formations; ICH, Indochina; MP, Malay Peninsula;
478 SIB, Sibumasu; SSh, Sunda Shelf; SUM, Sumatra; WS, West Sulawesi.

479

480 **Figure 2.** Eocene paleogeographic reconstruction, modified from *Golonka et al.* [2006] and
481 *Clements and Hall* [2011], highlighting the likely sources of sediments (Tin Belt Granites,
482 Schwaner Mountain Granitoids, etc.) and the likely sediment sinks (Crocker Fan, Java basins and
483 accretionary prism) from sedimentary provenance studies. Late Jurassic to Early Cretaceous red
484 beds are plotted from *Clements et al.* [2011]. Inferred paleo-drainage patterns (dark blue lines) for
485 the Eocene are shown only for schematic purposes. Brown arrows indicate the likely sedimentary
486 provenance across Sundaland.

487

488 **Figure 3.** Simplified schematic of basin histories for Southeast Asia synthesized from *Doust and*
489 *Sumner* [2007], including the changing tectonic and paleo-environmental settings recorded in the
490 sedimentary sequences. The regional unconformity across Sundaland was extracted from each basin
491 (red), highlighting the dominance of mid-Cretaceous to Eocene erosional environments on
492 Sundaland. The advance of shallow seas on Sundaland is recorded as the progression from
493 lacustrine environments during ~45–30 Ma to transgressive deltaic settings during ~30–22 Ma,
494 followed by fully marine environments until ~15 Ma. However, by ~15 Ma global sea levels had
495 fallen significantly due to growing inland ice sheets where long-term advance of flooding of

496 Sundaland was likely reversed. Full long-term exposure of Sundaland, as experienced in the latest
497 Cretaceous to Paleocene, has not occurred since ~15 Ma as demonstrated by continued deposition
498 of regressive deltaic sequences. Wavy lines represent unconformable contacts, many of which have
499 age uncertainties. Basin names and outlines are provided in Figure S1.

500

501 **Figure 4.** Paleo-environments interpreted from basin stratigraphy as age-coded by *Doust and*
502 *Sumner* [2007], attached to the plate reconstruction from *Zahirovic et al.* [2014], show progressive
503 flooding and sedimentary deposition in Sundaland basins since the Eocene. Plate boundaries and
504 velocities are presented as well as seafloor ages in shades of grey. IC – Indochina, SC – South
505 China, BOR – Borneo, WS – West Sulawesi, WB – West Burma, MP – Malay Peninsula, SIB –
506 Sibumasu, SSh – Sunda Shelf, (P)SCS – (Proto) South China Sea, PSP – Philippine Sea Plate.

507

508 **Figure 5.** Long-term continental inundation of Sundaland derived from *Golonka et al.* [2006].
509 Inundated continental areas (light blue) are most widespread in the Late Jurassic, Cretaceous and
510 post-Miocene times. Conversely, much of the continental area is emergent (orange) by Eocene
511 times, consistent with the widespread erosional/non-depositional regime on Sundaland that
512 represents the regional Late Cretaceous-Eocene unconformity [*Clements et al.*, 2011]. Post-Eocene
513 flooding propagated into the Sunda Shelf and the Gulf of Thailand, even though long-term eustatic
514 sea levels were falling during this time [*Haq and Al-Qahtani*, 2005; *Haq et al.*, 1987]. The input
515 paleogeographic maps are provided in Figure S2.

516

517 **Figure 6.** The large-scale mantle evolution from a 4D global numerical model of mantle flow using
518 CitcomS and visualised in GPlates. Time-dependent evolution of mantle flow coupled to the plate
519 reconstructions for Case 4, with subducting lithosphere (blue), and large-scale mantle upwelling
520 (red). The location of plate boundaries are plotted as white lines, subduction zones are thick yellow

521 regions, plate velocities are colored vectors and reconstructed present-day coastlines as white
522 translucent regions centred on Sundaland (S). See Animation S2.

523

524 **Figure 7.** Horizontally averaged (a) temperature and (b) temperature-dependent viscosity radial
525 profiles for Cases 1–4 at present-day.

526

527 **Figure 8.** Model dynamic topography and temperature as predicted by Case 4. A great circle profile
528 (thick black line) largely representative of the southern Sundaland active margin was reconstructed
529 in the plate frame of reference (i.e., Sumatra fixed). The evolution of mantle temperature is
530 represented on a vertical profile from the surface to the core-mantle boundary. The Early
531 Cretaceous tectonics of Sundaland is dominated by the northward subduction of the Meso-Tethys
532 (MT) and the southward subduction of Izanagi Plate along the Natuna and north Borneo active
533 margins to produce the East Asian slabs (EA) that interact with Tethyan slabs at depth. Rollback
534 and opening of the Woyla back-arc basin results in the formation of two independent Meso-Tethyan
535 slabs, followed by the onset of Woyla back-arc basin subduction (W) by ~100 Ma. The accretion of
536 West Sulawesi and East Java to Borneo by ~80 Ma interrupts subduction on eastern Sundaland,
537 while the collision of the Woyla terranes with Sumatra from ~75 Ma obstructs subduction for ~10–
538 15 Myr. Convergence and subduction is re-established along the Sunda segment (S) at ~65–60 Ma,
539 as indicated by the resumption of volcanism on Sumatra. The short-lived cessation of subduction
540 results in dynamic uplift during the Late Cretaceous to Eocene, while dynamic subsidence resumes
541 by ~40 Ma. PT, Paleo-Tethys slab. See Animation S3.

542

543 **Figure 9.** Present-day dynamic topography predicted by Cases 1–4 is plotted on the map panels in
544 (a–d), and superimposed with point estimates of residual topography from Winterbourne et al.
545 [2014] (symbols colored according to residual topography). Root-mean-square (RMS) distance
546 between predicted dynamic topography and the residual topography of *Winterbourne et al.* [2014]

547 is presented in the scatter plots. Symbols are colored according to the difference between dynamic
548 and residual topography. Circles are within one RMS, upward triangles are within two RMS, and
549 inverted triangles are beyond two RMS.

550

551 **Figure 10.** Comparison of model predictions with seismic tomography. The slab contours
552 representing mantle 10% colder than ambient for Cases 1–4 along a present-day transect (a) are
553 compared to (b–e), equivalent vertical slices of P- and S-wave tomographic models [*Grand, 2002*;
554 *Li et al., 2008*; *Obayashi et al., 2013*; *Ritsema et al., 2010*]. The Sunda slab (S) is predicted by all
555 models to a depth of ~1500 km, which is largely consistent with the tomographic models and earlier
556 interpretations [*Widiyantoro and van der Hilst, 1996*]. Importantly, the seismic tomography models
557 support the gap between the East Asian (EA) slabs in the lower mantle and the younger Sunda (S)
558 slab in the mid to upper mantle predicted by all four mantle flow models, and are a manifestation of
559 the ~80 to 65 Ma interruption of subduction along southern Sundaland. MT, Meso-Tethyan slabs.
560 BF, Bengal Fan; SCS, South China Sea.

561

562 **Figure 11.** Processes influencing the continental inundation of Sundaland. (a) The evolution of
563 long-term sea level (light and dark blue) with respect to present-day does not reproduce the flooding
564 history of Sundaland. (b) The trends from regionally-averaged dynamic topography with respect to
565 present-day (Cases 1 to 4) indicate a link between the emergence and flooding history of Sundaland
566 since the Late Cretaceous, in contrast to the eustatic trends. The light brown shading in the
567 background denotes widespread regional erosional environments likely responsible for the missing
568 sections of rock from sedimentary sequences (Figure 3).

569

570 **Figure 12.** Mean dynamic topography (DT). Average dynamic topography for Sundaland through
571 time in Cases 1 to 4 derived from sources of buoyancy deeper than 350 km (thick lines). For Case 4,
572 we also computed the dynamic topography from sources of buoyancy deeper than 250 km (dashed

573 thin green line), which highlights a higher amplitude of the dynamic topography prediction, while
574 maintaining the key trends of dynamic uplift between ~80–60 Ma and dynamic subsidence since
575 ~40 Ma. The thick lines are shifted in Figure 11b for the purpose of comparing trends in the
576 dynamic topography acting on Sundaland.

577

578

579 **Acknowledgements**

580 S.Z. was supported by an Australian Postgraduate Award, a University of Sydney Vice
581 Chancellor's Research Scholarship and ARC grant IH130200012. N.F. was supported by ARC
582 IH130200012. R.D.M. and M.S. were supported by ARC grants FL0992245 and FT130101564,
583 respectively. M.G. was partially supported by Statoil ASA and by the National Science Foundation
584 under grants CMMI-1028978, EAR-1161046 and EAR-1247022. We thank Sierd Cloetingh, Xi Liu
585 and Laurent Husson for constructive reviews that helped improve the manuscript. Figures were
586 constructed using Generic Mapping Tools [*Wessel and Smith, 1998; Wessel et al., 2013*], GPlates
587 (www.gplates.org) [*Boyden et al., 2011*], TimeScale Creator and ArcGIS. Numerical models were
588 carried out on the Sun Constellation VAYU cluster of the Australian National Computational
589 Infrastructure. The original *CitcomS* software was obtained from CIG, Computational Infrastructure
590 for Geodynamics (<http://geodynamics.org>). We thank J. Golonka and M. Pubellier for discussions
591 on regional and global paleogeographic and plate reconstructions. The data used are listed in the
592 references, tables, supplements and file repository at
593 ftp://ftp.earthbyte.org/Data_Collections/Zahirovic_etal_Sundaland_DynamicTopography.zip and
594 [ftp://ftp.earthbyte.org/Data_Collections/Muller_etal_2016_AREPS/Muller_etal_AREPS_Suppleme](ftp://ftp.earthbyte.org/Data_Collections/Muller_etal_2016_AREPS/Muller_etal_AREPS_Supplement.zip)
595 [nt.zip](ftp://ftp.earthbyte.org/Data_Collections/Muller_etal_2016_AREPS/Muller_etal_AREPS_Supplement.zip).

596

597

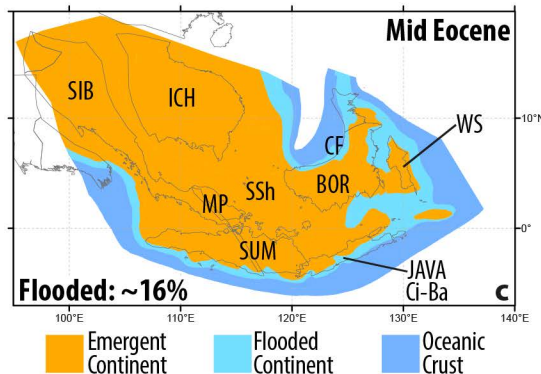
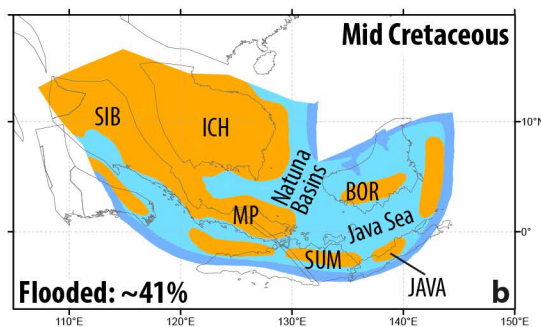
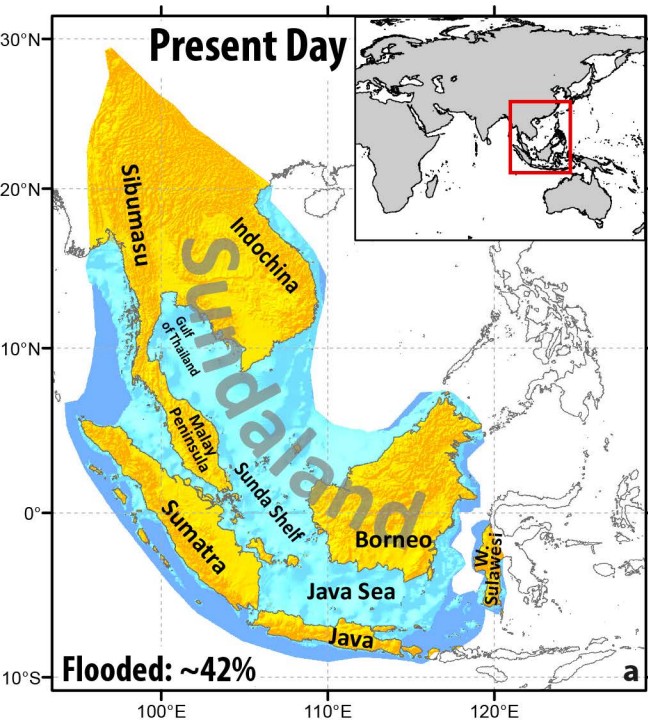
598 **References**

- 599 Becker, T., and L. Boschi (2002), A comparison of tomographic and geodynamic mantle models,
600 *Geochemistry, Geophysics, Geosystems*, 3(1), 1003.
- 601 Bertelloni, C. L., and M. Gurnis (1997), Cenozoic subsidence and uplift of continents from time-
602 varying dynamic topography, *Geology*, 25(8), 735-738.
- 603 Bower, D. J., M. Gurnis, and N. Flament (2015), Assimilating lithosphere and slab history in 4-D
604 Earth models, *Physics of the Earth and Planetary Interiors*, 238, 8-22, doi:
605 10.1016/j.pepi.2014.10.013.
- 606 Boyden, J., R. Müller, M. Gurnis, T. Torsvik, J. Clark, M. Turner, H. Ivey-Law, R. Watson, and J.
607 Cannon (2011), Next-generation plate-tectonic reconstructions using GPlates, in *Geoinformatics:
608 Cyberinfrastructure for the Solid Earth Sciences*, edited by G. Keller and C. Baru, pp. 95-114,
609 Cambridge University Press, Cambridge, UK.
- 610 Braun, J., X. Robert, and T. Simon - Labric (2013), Eroding dynamic topography, *Geophysical
611 Research Letters*, 40(8), 1494-1499, doi: 10.1002/grl.50310.
- 612 Buitter, S. J. H., R. Govers, and M. J. R. Wortel (2002), Two-dimensional simulations of surface
613 deformation caused by slab detachment, *Tectonophysics*, 354(3-4), 195-210, doi: 10.1016/S0040-
614 1951(02)00336-0.
- 615 Bunge, H.-P., C. Hagelberg, and B. Travis (2003), Mantle circulation models with variational data
616 assimilation: inferring past mantle flow and structure from plate motion histories and seismic
617 tomography, *Geophysical Journal International*, 152(2), 280-301.
- 618 Burgess, P. M., and M. Gurnis (1995), Mechanisms for the formation of cratonic stratigraphic
619 sequences, *Earth and Planetary Science Letters*, 136(3), 647-663, doi: 10.1016/0012-
620 821X(95)00204-P.
- 621 Clements, B., and R. Hall (2007), Cretaceous to Late Miocene stratigraphic and tectonic evolution
622 of West Java, *Indonesian Petroleum Association Proceedings*, 31(IPA07-G-037), 1-18.
- 623 Clements, B., and R. Hall (2011), A record of continental collision and regional sediment flux for
624 the Cretaceous and Palaeogene core of SE Asia: implications for early Cenozoic palaeogeography,
625 *Journal of the Geological Society*, 168, 1187-1200, doi: 10.1144/0016-76492011-004.
- 626 Clements, B., P. Burgess, R. Hall, and M. Cottam (2011), Subsidence and uplift by slab-related
627 mantle dynamics: a driving mechanism for the Late Cretaceous and Cenozoic evolution of
628 continental SE Asia?, *Geological Society, London, Special Publications*, 355(1), 37-51, doi:
629 10.1144/SP355.3
- 630 Colli, L., S. Ghelichkhan, and H. P. Bunge (2016), On the ratio of dynamic topography and gravity
631 anomalies in a dynamic Earth, *Geophysical Research Letters*.
- 632 Conrad, C. P., and M. Gurnis (2003), Seismic tomography, surface uplift, and the breakup of
633 Gondwanaland: Integrating mantle convection backwards in time, *Geochemistry, Geophysics,
634 Geosystems*, 4(3).
- 635 Conrad, C. P., and L. Husson (2009), Influence of dynamic topography on sea level and its rate of
636 change, *Lithosphere*, 1(2), 110-120.
- 637 Davies, J., and F. von Blanckenburg (1995), Slab breakoff: a model of lithosphere detachment and
638 its test in the magmatism and deformation of collisional orogens, *Earth and Planetary Science
639 Letters*, 129(1), 85-102, doi: 10.1016/0012-821X(94)00237-S.
- 640 Doust, H., and H. S. Sumner (2007), Petroleum systems in rift basins—a collective approach in
641 Southeast Asian basins, *Petroleum Geoscience*, 13(2), 127-144, doi: 10.1144/1354-079307-746.
- 642 Duretz, T., T. V. Gerya, and W. Spakman (2014), Slab detachment in laterally varying subduction
643 zones: 3-D numerical modeling, *Geophysical Research Letters*, 41(6), 1951-1956, doi:
644 10.1002/2014GL059472.
- 645 Flament, N., M. Gurnis, S. E. Williams, M. Seton, J. Skogseid, C. Heine, and R. D. Müller (2014),
646 Topographic asymmetry of the South Atlantic from global models of mantle flow and lithospheric
647 stretching, *Earth and Planetary Science Letters*, 387, 107-119, doi: 10.1016/j.epsl.2013.11.017.

- 648 Fuller, M., J. R. Ali, S. J. Moss, G. M. Frost, B. Richter, and A. Mahfi (1999), Paleomagnetism of
649 Borneo, *Journal of Asian Earth Sciences*, 17(1-2), 3-24, doi: 10.1016/S0743-9547(98)00057-9.
- 650 Golonka, J., M. Krobicki, J. Pajak, N. Van Giang, and W. Zuchiewicz (2006), *Global Plate*
651 *Tectonics and Paleogeography of Southeast Asia*, 128 pp., Faculty of Geology, Geophysics and
652 Environmental Protection, AGH University of Science and Technology, Arkadia, Krakow.
- 653 Grand, S. (2002), Mantle shear-wave tomography and the fate of subducted slabs, *Philosophical*
654 *Transactions of the Royal Society of London. Series A: Mathematical, Physical and Engineering*
655 *Sciences*, 360(1800), 2475.
- 656 Gudmundsson, Ó., and M. Sambridge (1998), A regionalized upper mantle (RUM) seismic model,
657 *Journal of Geophysical Research: Solid Earth*, 103(B4), 7121-7136.
- 658 Gurnis, M. (1991), Continental flooding and mantle-lithosphere dynamics, in *Glacial Isostasy, Sea-*
659 *Level and Mantle Rheology*, edited, pp. 445-492, Springer.
- 660 Gurnis, M. (1993), Phanerozoic marine inundation of continents driven by dynamic topography
661 above subducting slabs, doi: 10.1038/364589a0.
- 662 Gurnis, M., R. Müller, and L. Moresi (1998), Cretaceous vertical motion of Australia and the
663 Australian Antarctic discordance, *Science*, 279(5356), 1499-1504, doi:
664 10.1126/science.279.5356.1499.
- 665 Hager, B., R. Clayton, M. Richards, R. Comer, and A. Dziewonski (1985), Lower mantle
666 heterogeneity, dynamic topography and the geoid, *Nature*, 313(6003), 541-545.
- 667 Hall, R. (2002), Cenozoic geological and plate tectonic evolution of SE Asia and the SW Pacific:
668 computer-based reconstructions, model and animations, *Journal of Asian Earth Sciences*, 20(4),
669 353-431, doi: 10.1016/S0012-821X(04)00070-6.
- 670 Hall, R., and W. Spakman (2015), Mantle structure and tectonic history of SE Asia, *Tectonophysics*,
671 658, 14-45, doi: 10.1016/j.tecto.2015.07.003.
- 672 Haq, B. U. (2014), Cretaceous eustasy revisited, *Global and Planetary Change*, 113, 44-58, doi:
673 10.1016/j.gloplacha.2013.12.007.
- 674 Haq, B. U., and A. M. Al-Qahtani (2005), Phanerozoic cycles of sea-level change on the Arabian
675 Platform, *GeoArabia*, 10(2), 127-160.
- 676 Haq, B. U., J. Hardenbol, and P. R. Vail (1987), Chronology of fluctuating sea levels since the
677 Triassic, *Science*, 235(4793), 1156-1167, doi: 10.1126/science.235.4793.1156
- 678 Hoggard, M., N. White, and D. Al-Attar (2016), Global dynamic topography observations reveal
679 limited influence of large-scale mantle flow, *Nature Geoscience*.
- 680 Hutchison, C. S. (1975), Ophiolite in Southeast Asia, *Geological Society of America Bulletin*, 86(6),
681 797-806, doi: 10.1130/0016-7606(1975)86<797:OISA>2.0.CO;2.
- 682 Hutchison, C. S. (1996), The 'Rajang accretionary prism' and 'Lupar Line' problem of Borneo,
683 *Geological Society, London, Special Publications*, 106(1), 247-261, doi:
684 10.1144/GSL.SP.1996.106.01.16.
- 685 Hutchison, C. S. (2010), Oroclines and paleomagnetism in Borneo and South-East Asia,
686 *Tectonophysics*, 496(1), 53-67, doi: 10.1016/j.tecto.2010.10.008.
- 687 Kárason, H. (2002), Constraints on Mantle Convection from Seismic
688 Tomography and Flow Modeling, Massachusetts Institute of Technology.
- 689 Katili, J. A. (1975), Volcanism and plate tectonics in the Indonesian island arcs, *Tectonophysics*,
690 26(3), 165-188, doi: 10.1016/0040-1951(75)90088-8.
- 691 Lee, T.-Y., and L. A. Lawver (1995), Cenozoic plate reconstruction of Southeast Asia,
692 *Tectonophysics*, 251(1-4), 85-138, doi: 10.1016/0040-1951(95)00023-2.
- 693 Li, C., R. van der Hilst, E. Engdahl, and S. Burdick (2008), A new global model for P wave speed
694 variations in Earth's mantle, *Geochemistry, Geophysics, Geosystems*, 9(5), 21, Q05018, doi:
695 10.1029/2007GC001806.
- 696 Li, Z. H., Z. Xu, T. Gerya, and J.-P. Burg (2013), Collision of continental corner from 3-D
697 numerical modeling, *Earth and Planetary Science Letters*, 380, 98-111.

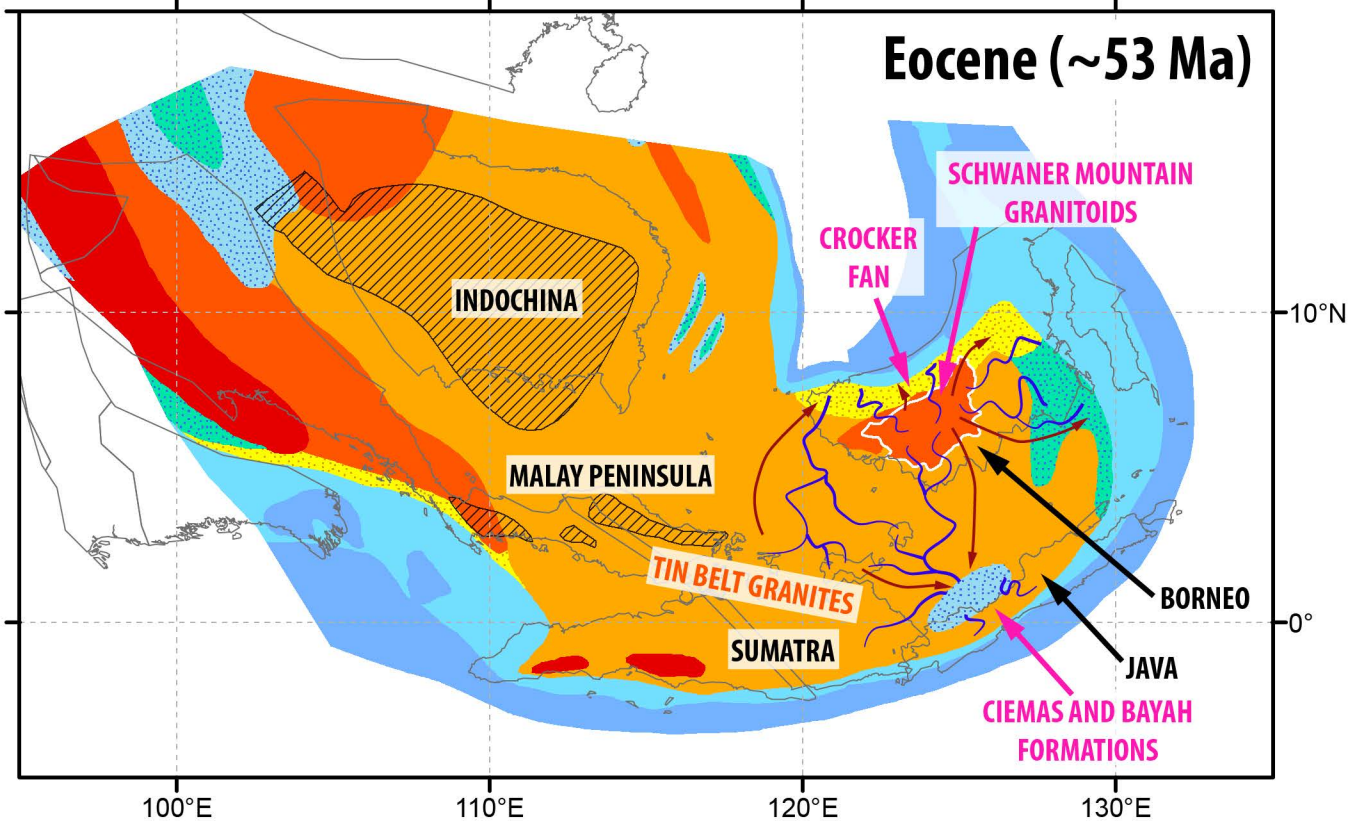
- 698 Lovell, B. (2010), A pulse in the planet: regional control of high-frequency changes in relative sea
699 level by mantle convection, *Journal of the Geological Society*, 167(4), 637-648, doi: 10.1144/0016-
700 76492009-127.
- 701 McCourt, W., M. Crow, E. Cobbing, and T. Amin (1996), Mesozoic and Cenozoic plutonic
702 evolution of SE Asia: evidence from Sumatra, Indonesia, *Geological Society, London, Special
703 Publications*, 106(1), 321-335, doi: 10.1144/GSL.SP.1996.106.01.21.
- 704 McKenzie, D. (2010), The influence of dynamically supported topography on estimates of T_e ,
705 *Earth and Planetary Science Letters*, 295(1), 127-138, doi: 10.1016/j.epsl.2010.03.033.
- 706 Metcalfe, I. (1988), Origin and assembly of south-east Asian continental terranes, *Geological
707 Society, London, Special Publications*, 37(1), 101-118, doi: 10.1144/GSL.SP.1988.037.01.08
- 708 Moucha, R., A. M. Forte, J. X. Mitrovica, D. B. Rowley, S. Quéré, N. A. Simmons, and S. P. Grand
709 (2008), Dynamic topography and long-term sea-level variations: There is no such thing as a stable
710 continental platform, *Earth and Planetary Science Letters*, 271(1), 101-108, doi:
711 10.1016/j.epsl.2008.03.056.
- 712 Müller, R., M. Sdrolias, C. Gaina, B. Steinberger, and C. Heine (2008), Long-term sea-level
713 fluctuations driven by ocean basin dynamics, *science*, 319(5868), 1357.
- 714 Müller, R. D., et al. (2016), Ocean basin evolution and global-scale plate reorganization events
715 since Pangea breakup, *Annual Review of Earth and Planetary Sciences*, 44.
- 716 Obayashi, M., J. Yoshimitsu, G. Nolet, Y. Fukao, H. Shiobara, H. Sugioka, H. Miyamachi, and Y.
717 Gao (2013), Finite frequency whole mantle P wave tomography: Improvement of subducted slab
718 images, *Geophysical Research Letters*, 40(21), 5652-5657, doi: 10.1002/2013GL057401.
- 719 Replumaz, A., H. Karason, R. D. van der Hilst, J. Besse, and P. Tapponnier (2004), 4-D evolution
720 of SE Asia's mantle from geological reconstructions and seismic tomography, *Earth and Planetary
721 Science Letters*, 221(1-4), 103-115.
- 722 Ritsema, J., A. Deuss, H. Van Heijst, and J. Woodhouse (2010), S40RTS: a degree- 40 shear-
723 velocity model for the mantle from new Rayleigh wave dispersion, teleseismic traveltime and
724 normal-mode splitting function measurements, *Geophysical Journal International*, doi:
725 10.1111/j.1365-246X.2010.04884.x.
- 726 Ritsema, J., A. Deuss, H. Van Heijst, and J. Woodhouse (2011), S40RTS: a degree-40 shear-
727 velocity model for the mantle from new Rayleigh wave dispersion, teleseismic traveltime and
728 normal-mode splitting function measurements, *Geophysical Journal International*, 184(3), 1223-
729 1236.
- 730 Romanowicz, B. (2003), Global mantle tomography: progress status in the past 10 years, *Annual
731 Review of Earth and Planetary Sciences*, 31(1), 303-328.
- 732 Romanowicz, B. (2008), Using seismic waves to image Earth's internal structure, *Nature*,
733 451(7176), 266-268.
- 734 Seton, M., C. Gaina, R. D. Müller, and C. Heine (2009), Mid-Cretaceous seafloor spreading pulse:
735 Fact or fiction?, *Geology*, 37(8), 687-690, doi: 10.1130/G25624A.1
- 736 Seton, M., et al. (2012), Global continental and ocean basin reconstructions since 200 Ma, *Earth-
737 Science Reviews*, 113(3-4), 212-270, doi: 10.1016/j.earscirev.2012.03.002.
- 738 Soeria-Atmadja, R., D. Noeradi, and B. Priadi (1999), Cenozoic magmatism in Kalimantan and its
739 related geodynamic evolution, *Journal of Asian Earth Sciences*, 17(1), 25-45, doi: 10.1016/S0743-
740 9547(98)00062-2.
- 741 Spasojevic, S., and M. Gurnis (2012), Sea level and vertical motion of continents from dynamic
742 earth models since the Late Cretaceous, *AAPG bulletin*, 96(11), 2037-2064, doi:
743 10.1306/03261211121.
- 744 Steinberger, B., and A. R. Calderwood (2006), Models of large-scale viscous flow in the Earth's
745 mantle with constraints from mineral physics and surface observations, *Geophysical Journal
746 International*, 167(3), 1461-1481, doi: 10.1111/j.1365-246X.2006.03131.x.
- 747 Steinberger, B., and T. H. Torsvik (2008), Absolute plate motions and true polar wander in the
748 absence of hotspot tracks, *Nature*, 452(7187), 620-623, doi: 10.1038/nature06824.






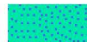



- 749 Torsvik, T., R. Müller, R. Van der Voo, B. Steinberger, and C. Gaina (2008), Global plate motion
750 frames: toward a unified model, *Reviews of Geophysics*, 46(3), doi: 10.1029/2007RG000227.
- 751 Vail, P. R., R. Mitchum Jr, and S. Thompson III (1977), Seismic Stratigraphy and Global Changes
752 of Sea Level: Part 4. Global Cycles of Relative Changes of Sea Level.: Section 2. Application of
753 Seismic Reflection Configuration to Stratigraphic Interpretation, in *Seismic Stratigraphy -
754 Applications to Hydrocarbon Exploration*, edited, AAPG Memoir 26.
- 755 van der Meer, D. G., W. Spakman, D. J. van Hinsbergen, M. L. Amaru, and T. H. Torsvik (2010),
756 Towards absolute plate motions constrained by lower-mantle slab remnants, *Nature Geoscience*,
757 3(1), 36-40, doi: 10.1038/ngeo708.
- 758 van Hattum, M. W., R. Hall, A. L. Pickard, and G. J. Nichols (2006), Southeast Asian sediments not
759 from Asia: Provenance and geochronology of north Borneo sandstones, *Geology*, 34(7), 589-592,
760 doi: 10.1130/G21939.1.
- 761 van Hunen, J., and M. B. Allen (2011), Continental collision and slab break-off: a comparison of 3-
762 D numerical models with observations, *Earth and Planetary Science Letters*, 302(1), 27-37.
- 763 Wessel, P., and W. H. Smith (1998), New, improved version of Generic Mapping Tools released,
764 *Eos, Transactions American Geophysical Union*, 79(47), 579-579, doi: 10.1029/98EO00426.
- 765 Wessel, P., W. H. Smith, R. Scharroo, J. Luis, and F. Wobbe (2013), Generic Mapping Tools:
766 Improved Version Released, *Eos, Transactions American Geophysical Union*, 94(45), 409-410, doi:
767 10.1002/2013EO450001.
- 768 Whittaker, J., R. Müller, M. Sdrolias, and C. Heine (2007), Sunda-Java trench kinematics, slab
769 window formation and overriding plate deformation since the Cretaceous, *Earth and Planetary
770 Science Letters*, 255(3), 445-457, doi: 10.1016/j.epsl.2006.12.031.
- 771 Widiyantoro, S., and R. D. van der Hilst (1996), Structure and evolution of subducted lithosphere
772 beneath the Sunda arc, Indonesia, *Science Reports*, 271(5255), 1566-1570.
- 773 Wilson, M. E., and S. J. Moss (1999), Cenozoic palaeogeographic evolution of Sulawesi and
774 Borneo, *Palaeogeography, Palaeoclimatology, Palaeoecology*, 145(4), 303-337.
- 775 Winterbourne, J., N. White, and A. Crosby (2014), Accurate measurements of residual topography
776 from the oceanic realm, *Tectonics*, 33, 982-1015, doi: 10.1002/2013TC003372.
- 777 Wright, N., S. Zahirovic, R. D. Müller, and M. Seton (2013), Towards community-driven
778 paleogeographic reconstructions: integrating open-access paleogeographic and paleobiology data
779 with plate tectonics, *Biogeosciences*, 10(3), 1529-1541, doi: 10.5194/bg-10-1529-2013.
- 780 Wu, J., J. Suppe, R. Lu, and R. Kanda (2016), Philippine Sea and East Asian plate tectonics since
781 52 Ma constrained by new subducted slab reconstruction methods, *Journal of Geophysical
782 Research: Solid Earth*, doi: 10.1002/2016JB012923.
- 783 Yang, T., M. Gurnis, and S. Zahirovic (2016), Mantle - induced subsidence and compression in SE
784 Asia since the early Miocene, *Geophysical Research Letters*, doi: 10.1002/2016GL068050.
- 785 Zahirovic, S., M. Seton, and R. D. Müller (2014), The Cretaceous and Cenozoic tectonic evolution
786 of Southeast Asia, *Solid Earth (EGU)*, 5, 227-273, doi: 10.5194/se-5-227-2014.
- 787 Zhong, S., A. McNamara, E. Tan, L. Moresi, and M. Gurnis (2008), A benchmark study on mantle
788 convection in a 3 - D spherical shell using CitcomS, *Geochemistry, Geophysics, Geosystems*, 9(10).
789
790
-

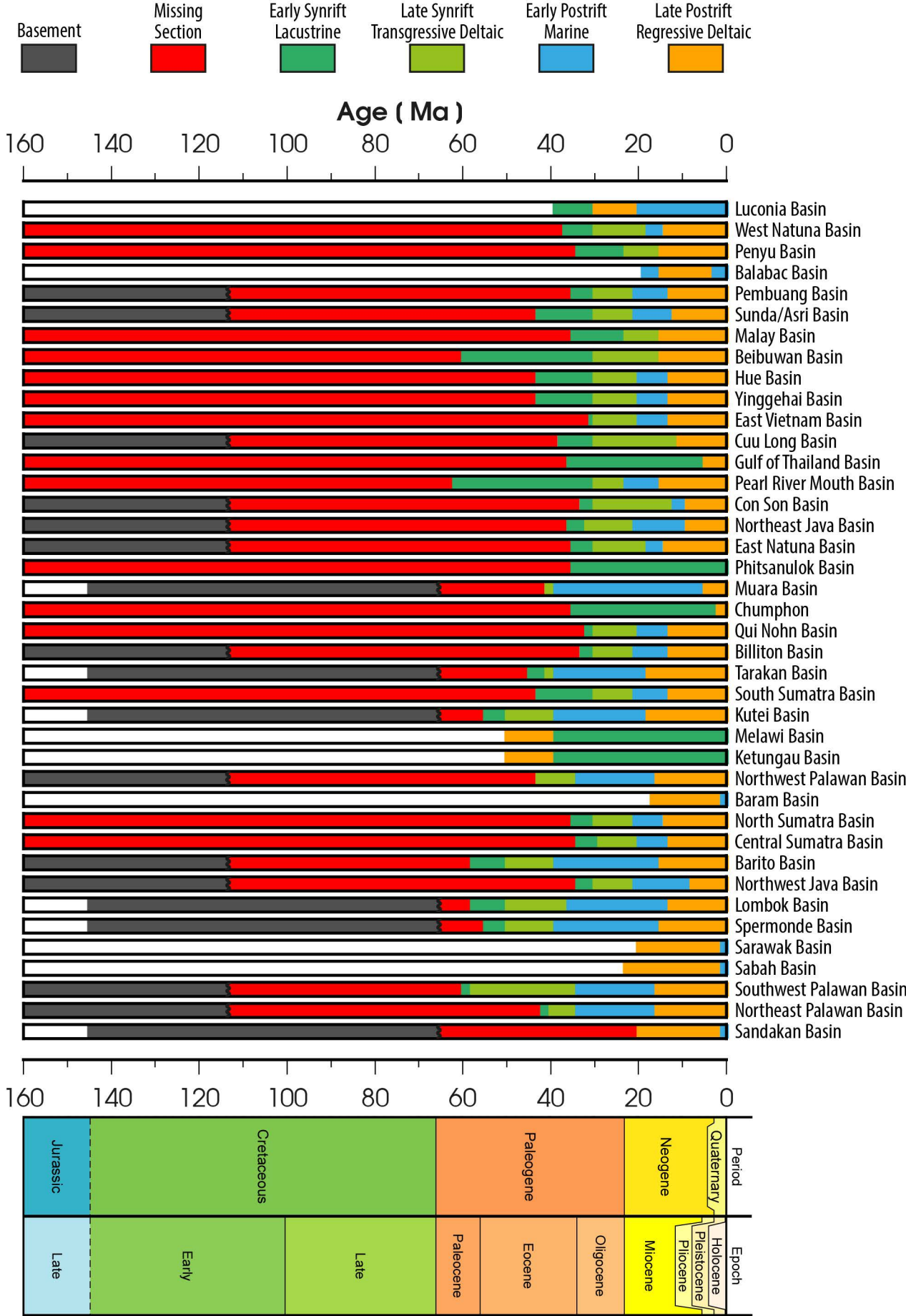


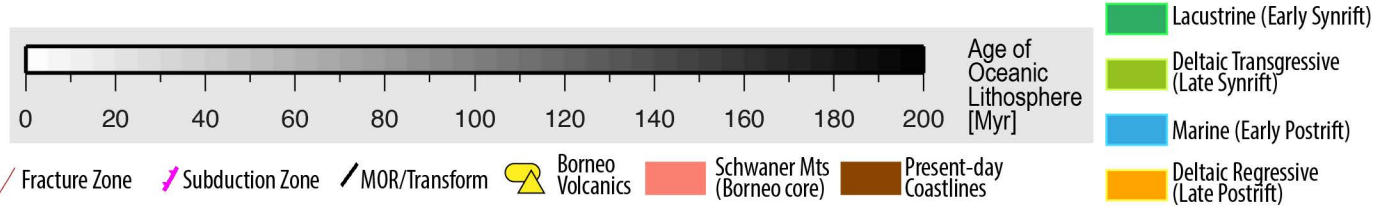
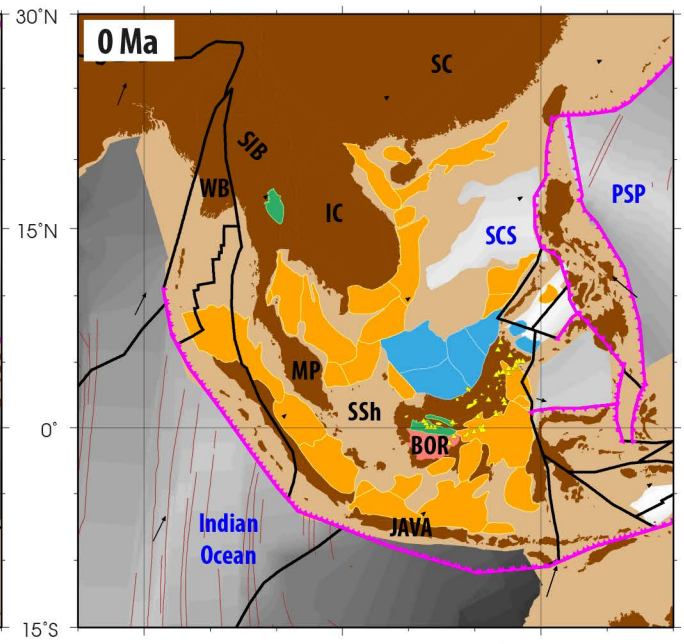
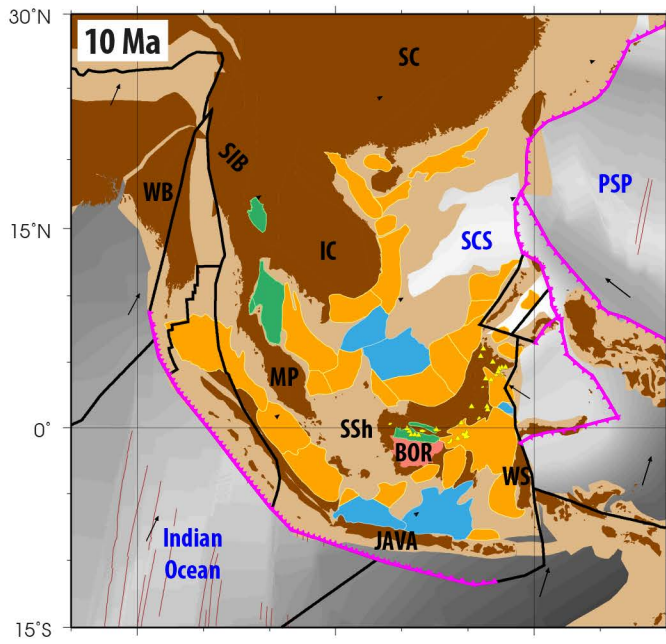
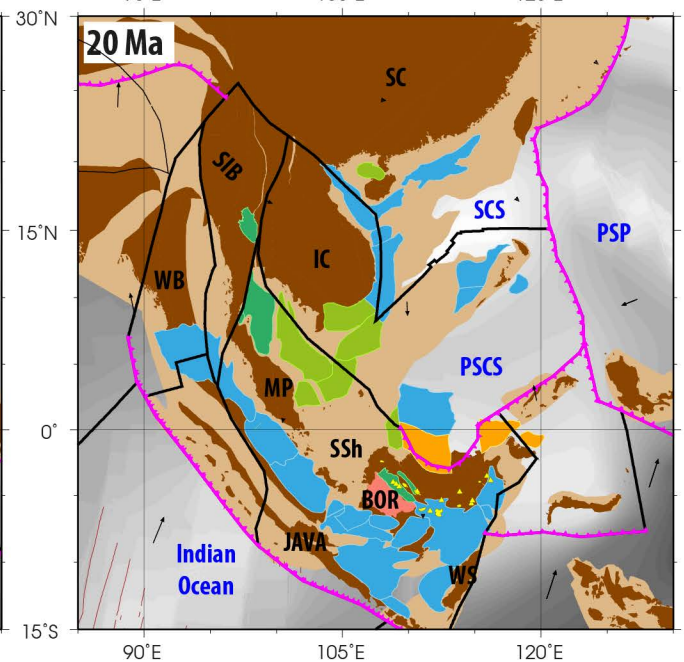
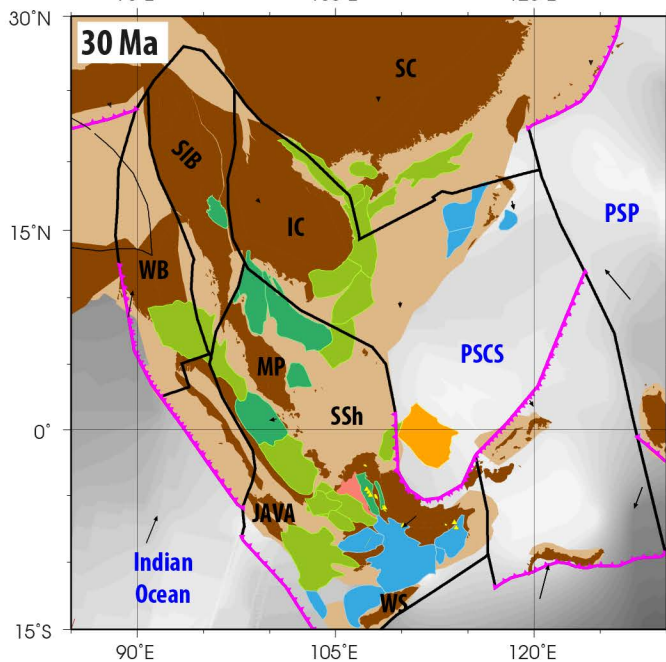
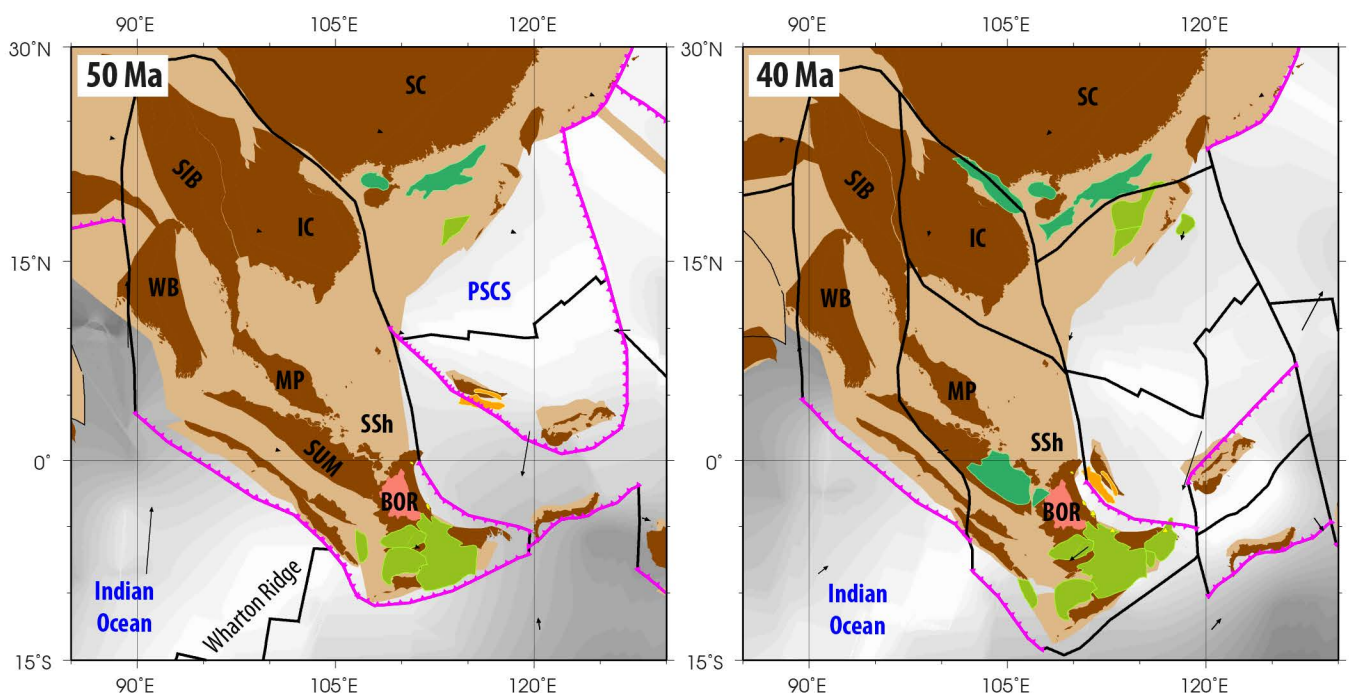
Emergent Continent
 Flooded Continent
 Oceanic Crust

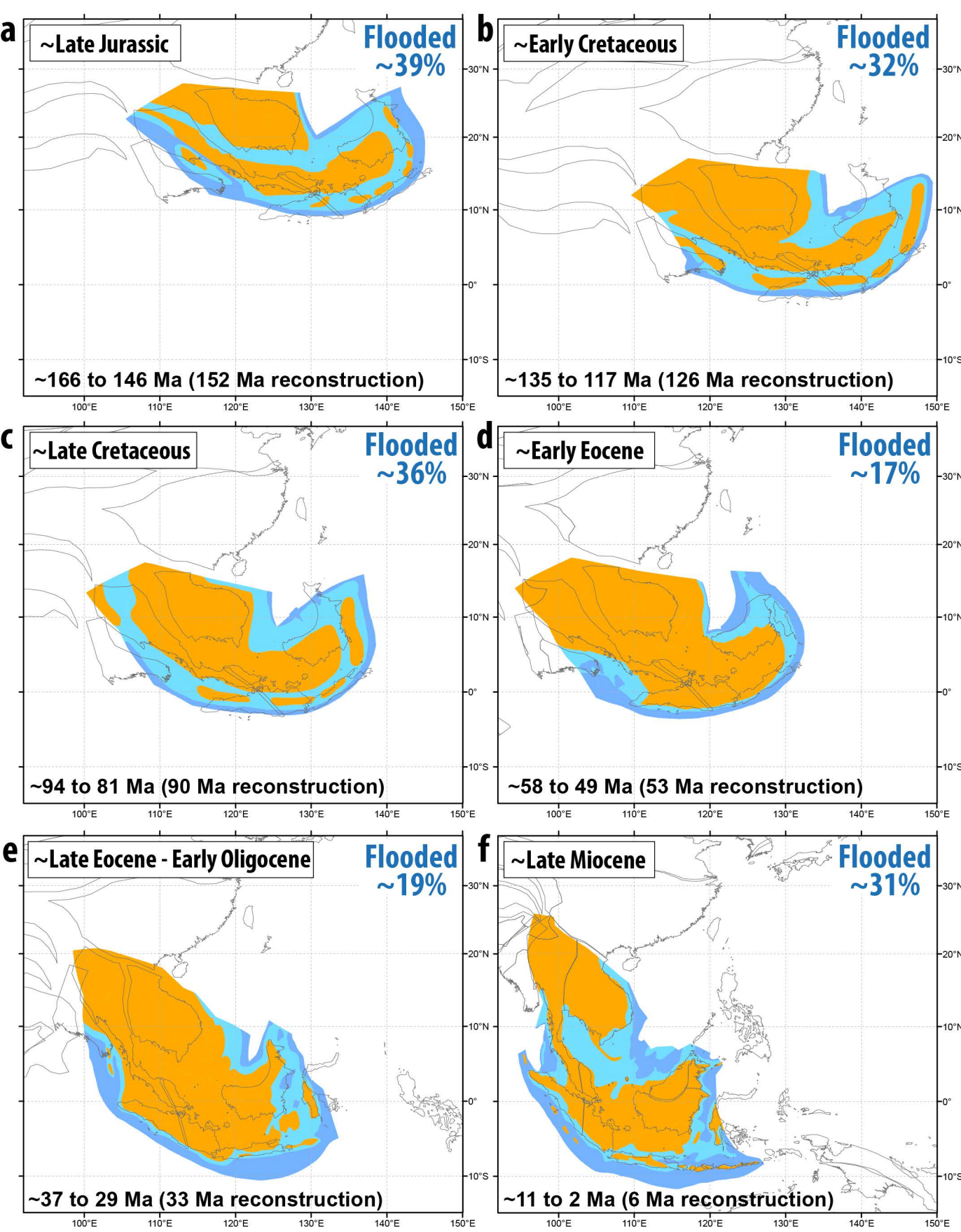
Eocene (~53 Ma)



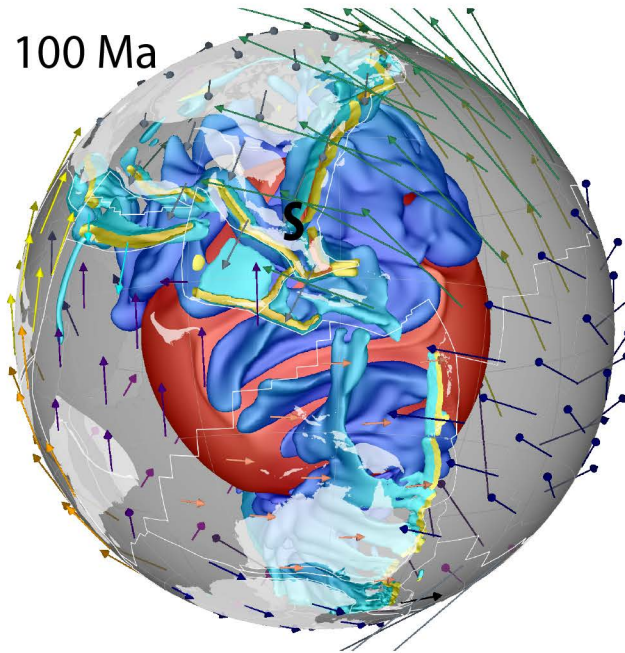
- | | | | |
|--|--|---|---|
|  | Mountains and Highlands (active deformation) |  | Coastal, Transitional and Marginal Marine |
|  | Topographic High (little tectonic deformation) |  | Fluvial |
|  | Emergent Land (erosional) |  | Fluvio - Lacustrine |
|  | Shallow Marine (continental shelf) |  | Late Jurassic red beds |
|  | Deep Marine (non-continental) | | |



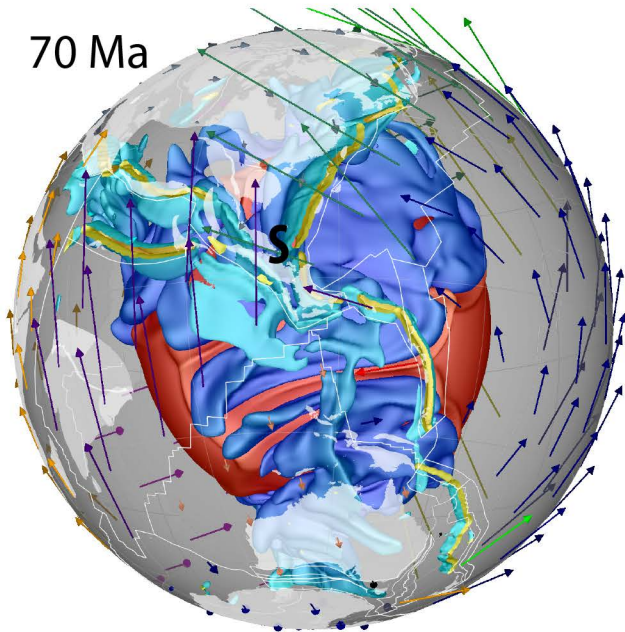




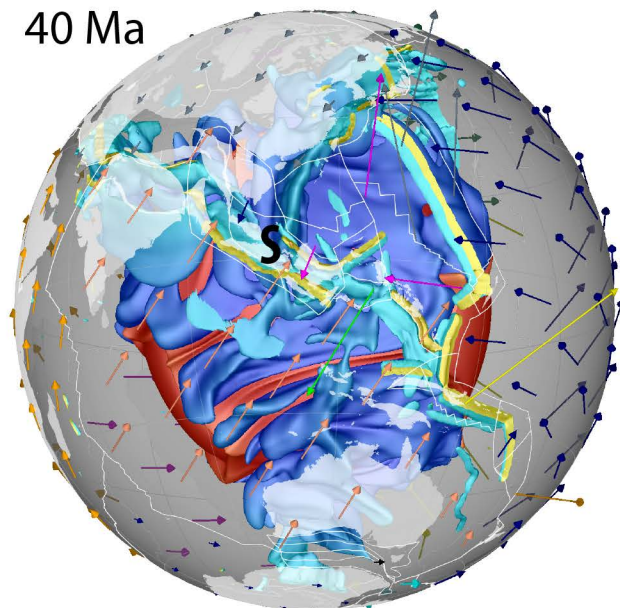
100 Ma



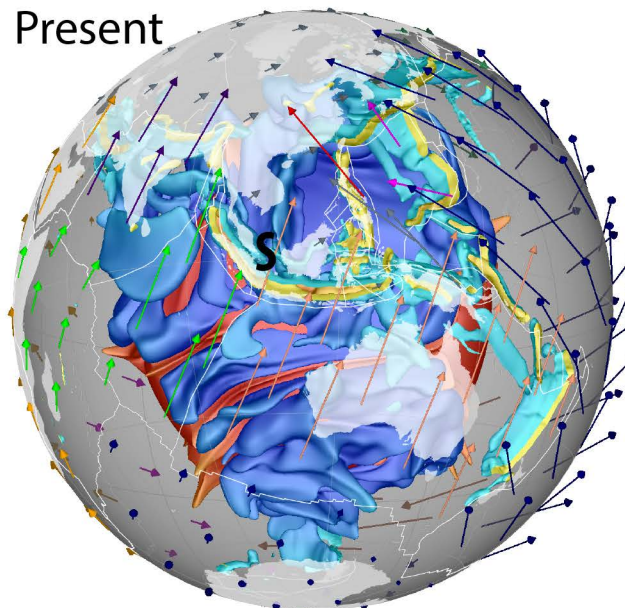
70 Ma

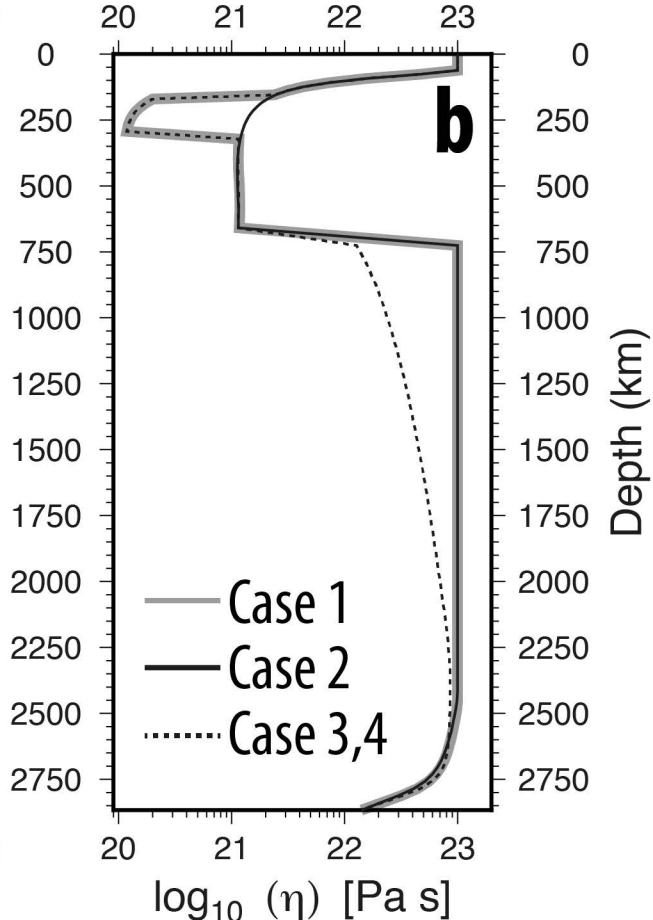
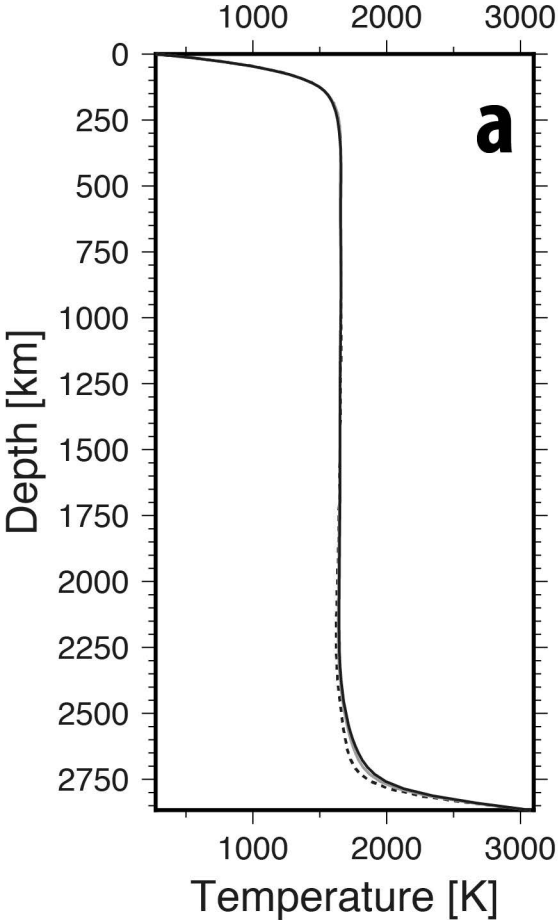


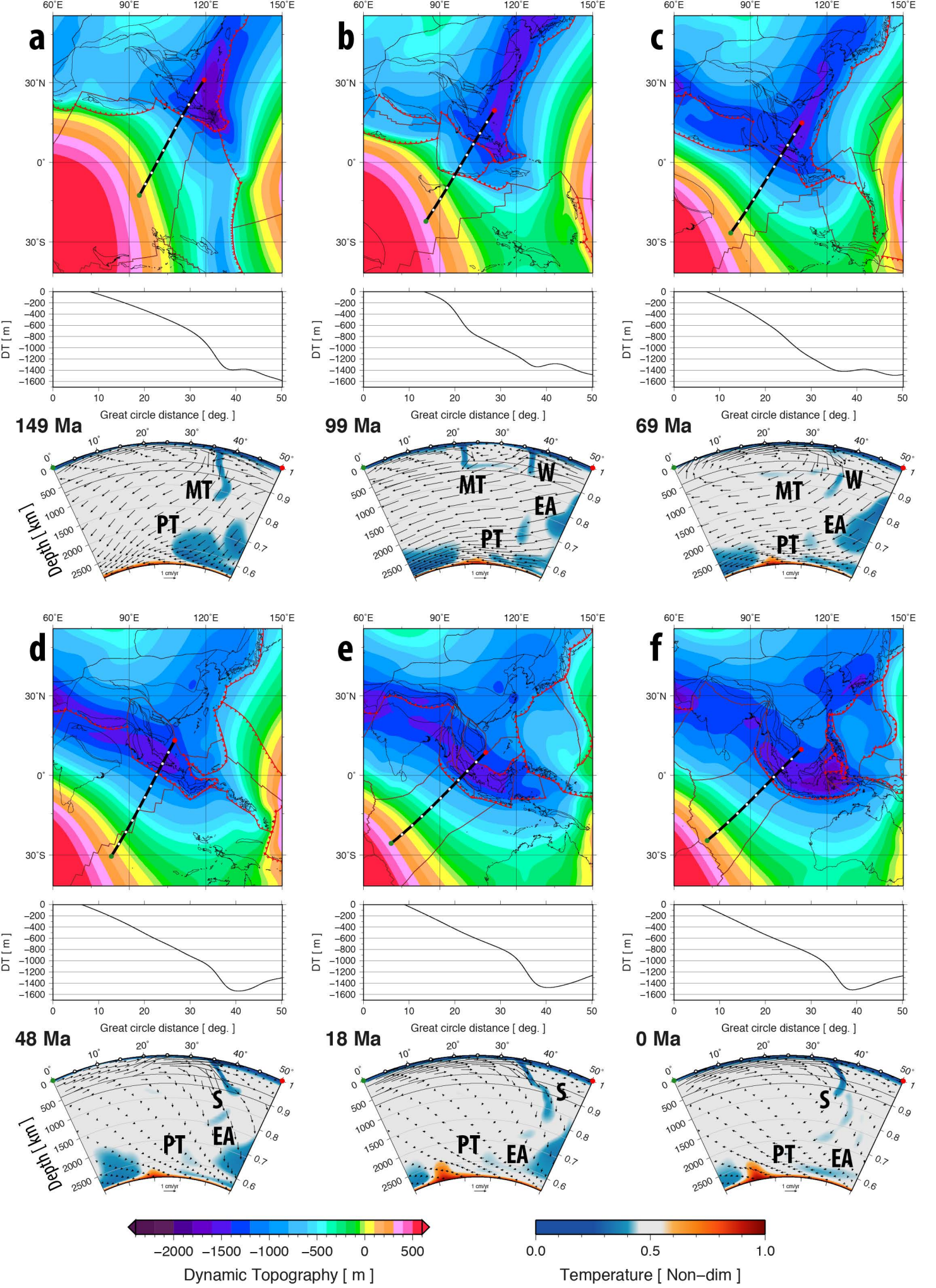
40 Ma

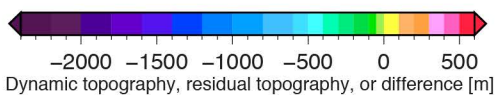
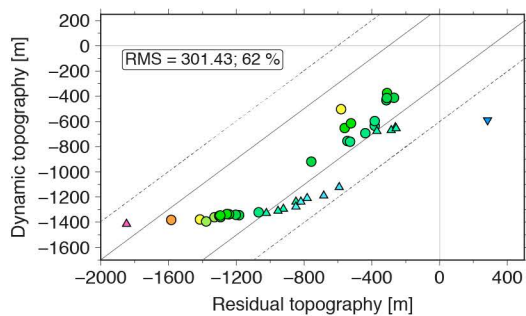
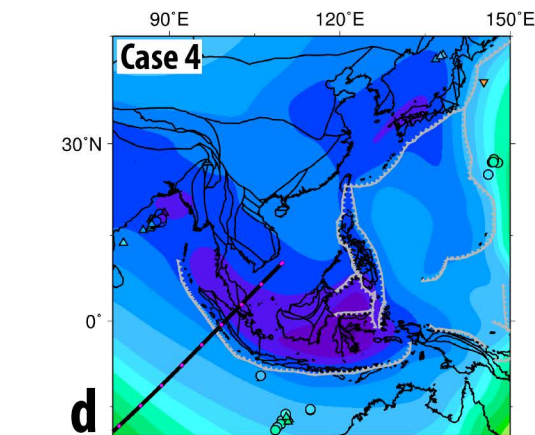
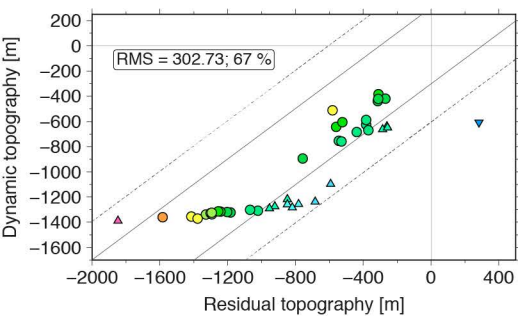
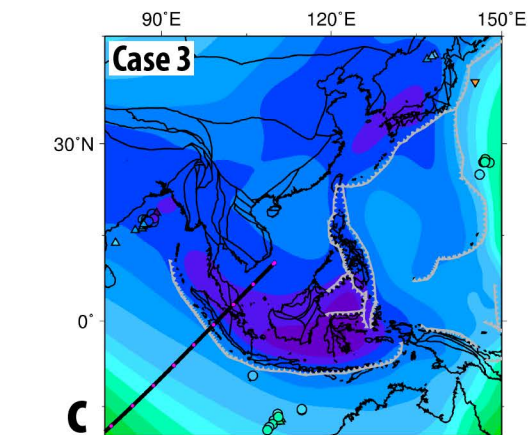
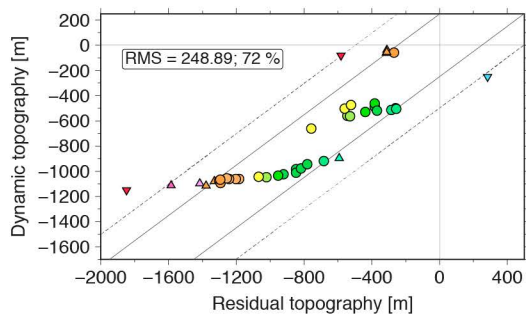
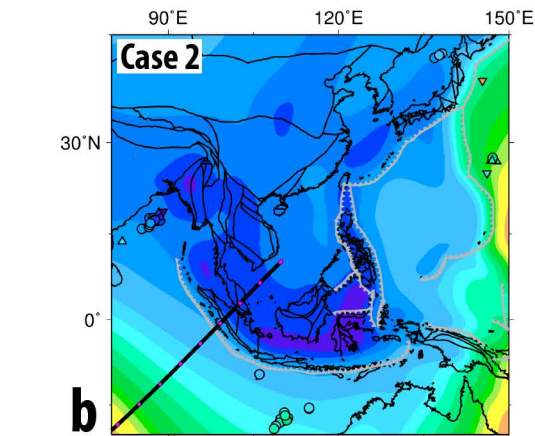
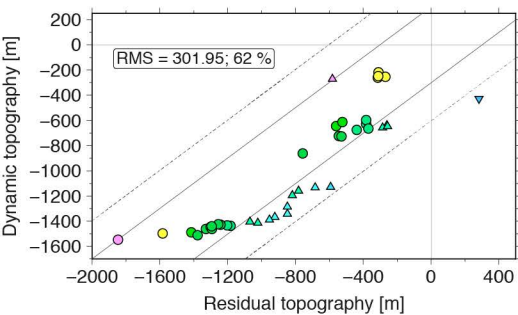
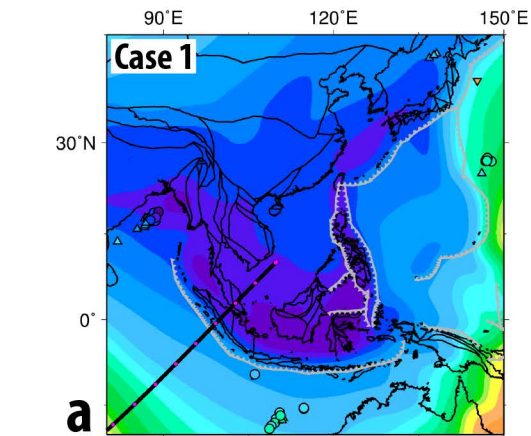


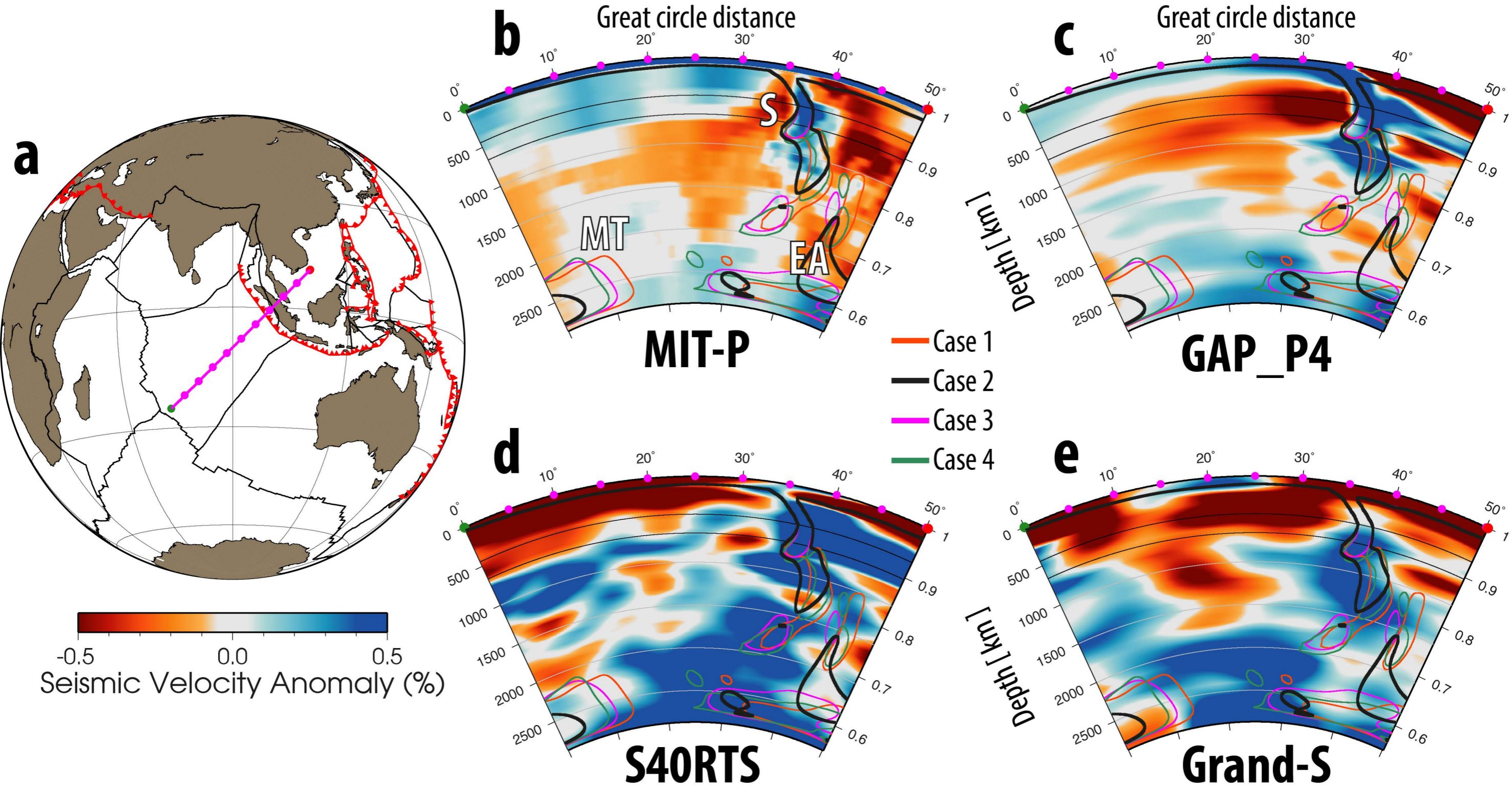
Present

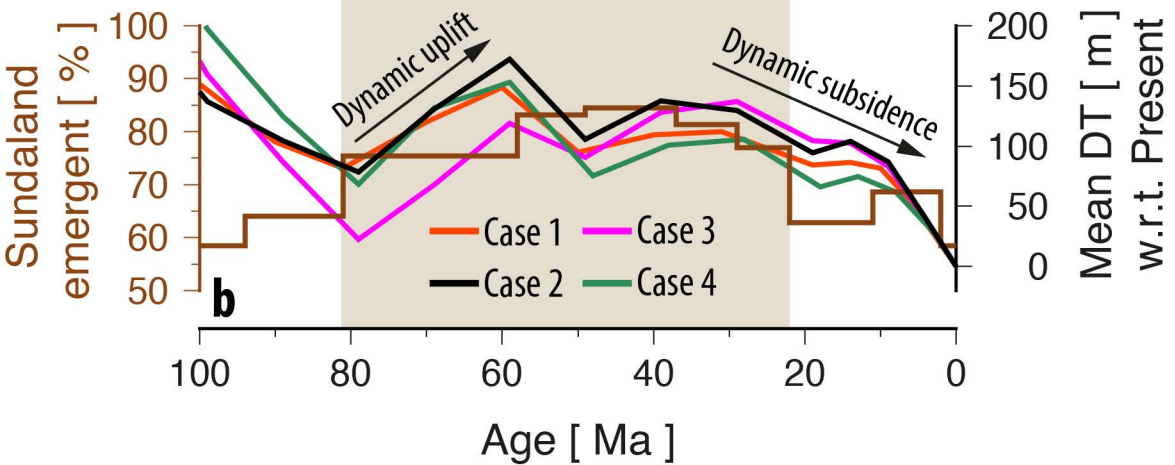
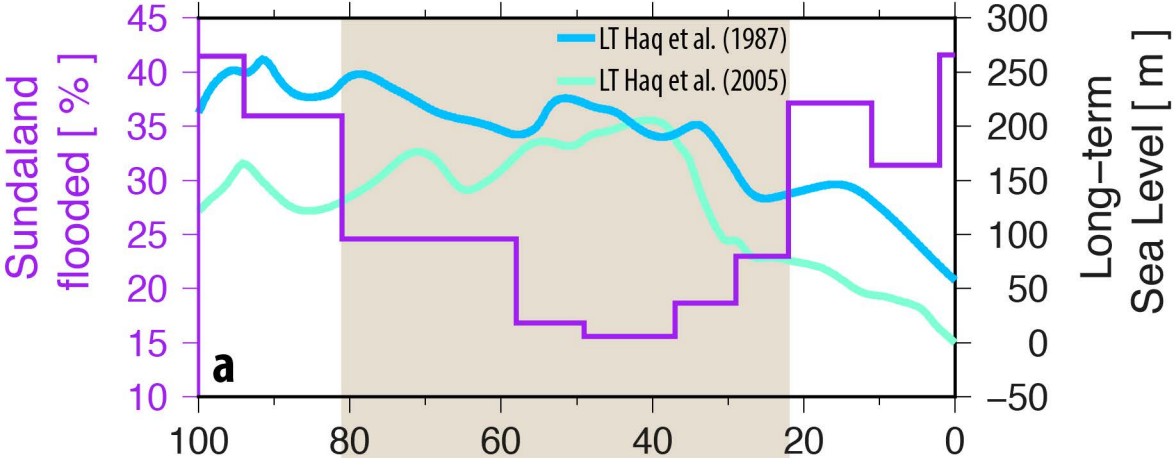


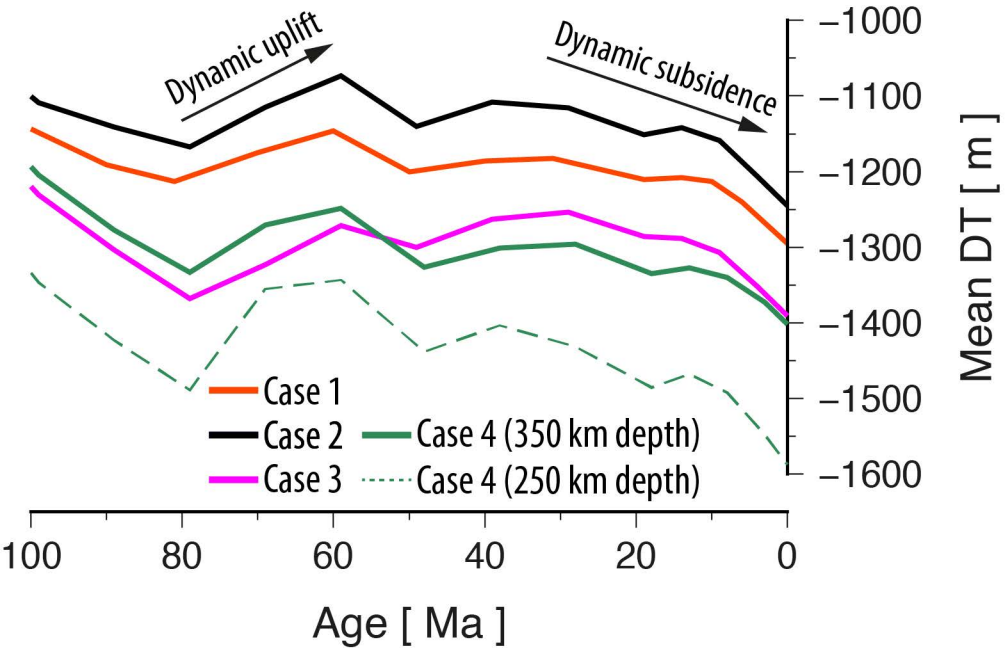












Large fluctuations of shallow seas in low-lying Southeast Asia driven by mantle flow

Sabin Zahirovic¹, Nicolas Flament¹, R Dietmar Müller¹, Maria Seton¹, and Michael Gurnis²

¹EarthByte Group, School of Geosciences, The University of Sydney, NSW 2006, Australia

²Seismological Laboratory, California Institute of Technology, Pasadena, California 91125, USA

Contents of this file

Figures S1 to S2

Additional Supporting Information (Files uploaded separately)

Captions for Movies S1 to S3

Introduction

The supporting information includes two figures and explanations of the digital datasets and associated animation files.

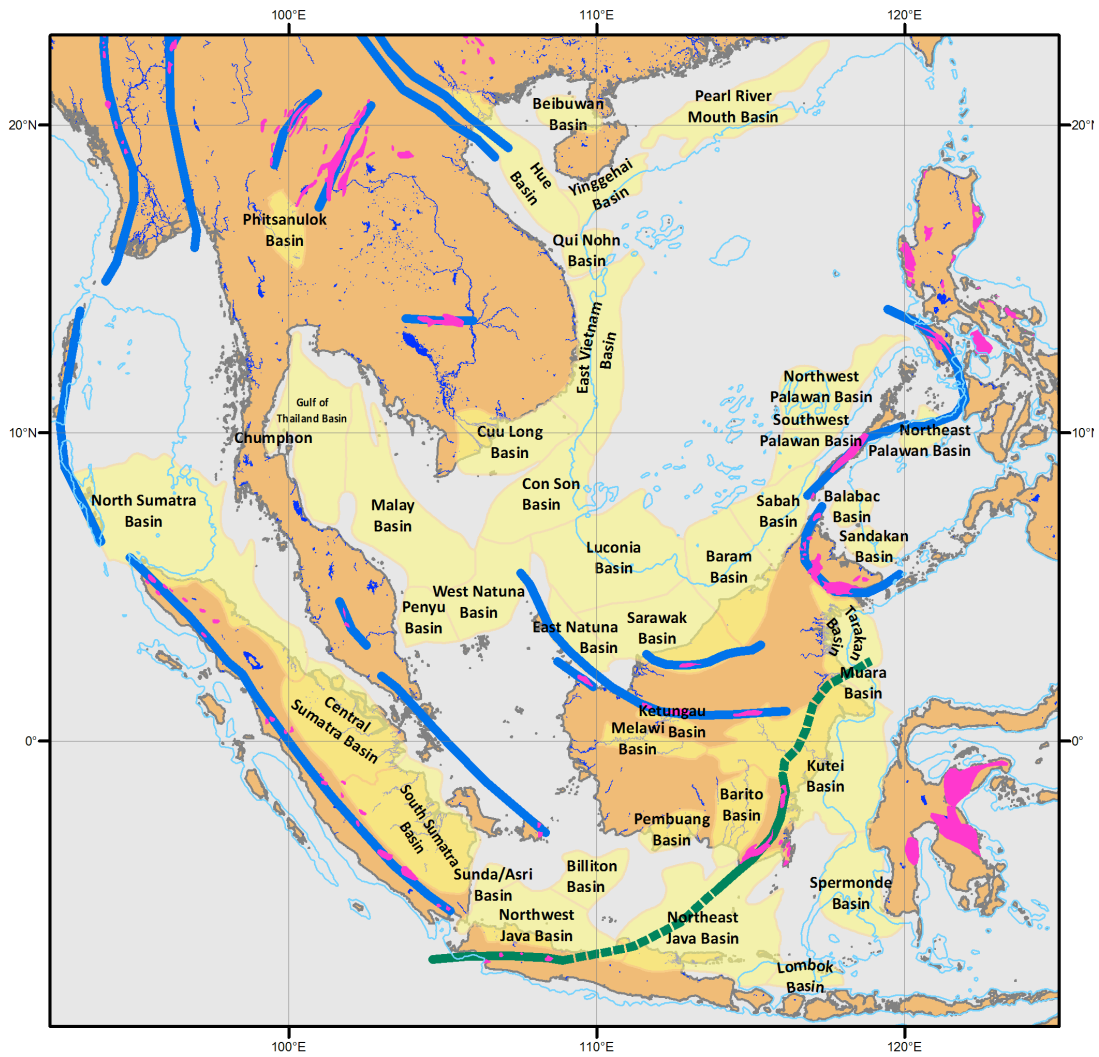


Figure S1. Distribution of sedimentary basins (yellow) across Sundaland, adapted from *Zahirovic et al.* [2014]. Thick blue and green lines represent sutures, and magenta polygons represent ophiolite exposures. Thin blue lines and polygons represent present-day fluvial and lacustrine systems.

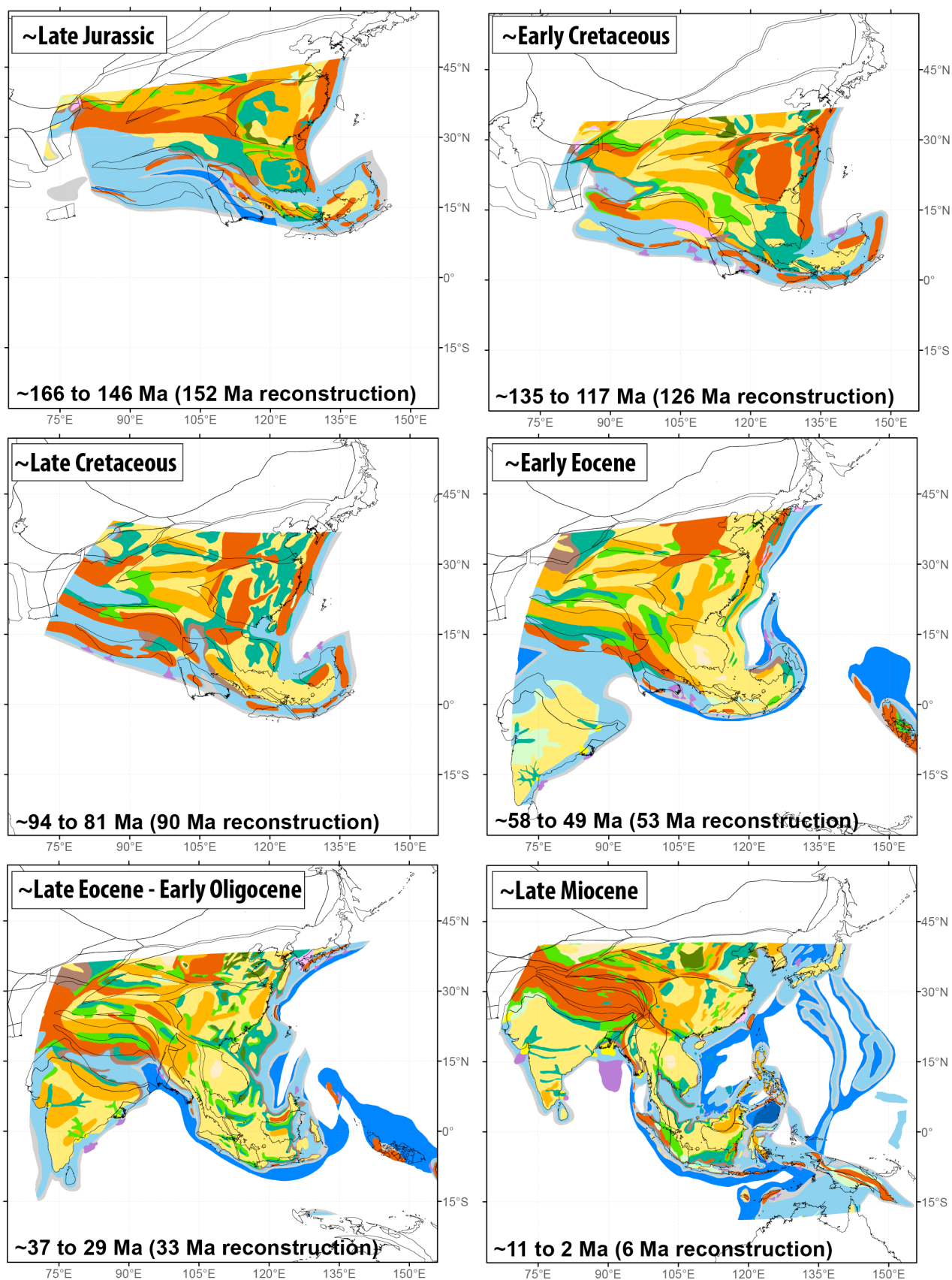


Figure S2. The paleogeographic maps from *Golonka et al.* [2006] georeferenced in a similar relative plate motion model presented in *Wright et al.* [2013]. Orange and red represent mountains. Yellow represents emergent land, and green regions represent terrestrial and/or lacustrine environments. Light blue represents continental shelves, and deep blue represents deeper marine environments. Grey represents

continental slopes, and purple represents large fluvial fan systems. Detailed key to colors is provided in *Golonka et al. [2006]*.

Movie S1. Animation of basin paleo-environments embedded in a plate tectonic reconstruction as in Figure 4.

Movie S2. 4D animation of mantle flow model from Case 4 as in Figure 6.

Movie S3. Animation of the vertical slice from Case 4 as in Figure 8.

Data Set S1. Sundaland flooding curve (percentage of flooded continental crust).

Data Set S2. Set of GPlates-compatible polygons whose intersections can be used to re-create the regions we extracted to compute the average dynamic topography for Sundaland.